

Observation of Robust and Coherent Non-Abelian Hadron Dynamics on Noisy Quantum Processors

Fran Ilčić^{1,*}, Ritajit Majumdar^{2,*}, Emil Mathew^{1,*}, Md. Osama Ali¹,
Nathan Earnest-Noble³ & Indrakshi Raychowdhury¹

¹Department of Physics and Center for Research in Quantum Information and Technology,

Birla Institute of Technology and Science Pilani,
K K Birla Goa Campus, Zuarinagar, Sancole, Goa 403726, India.

²IBM Quantum, IBM India Research Lab, India.

³IBM Quantum, IBM T.J. Watson Research Center, Yorktown Heights, NY 10598, USA.

* contributed equally.

The real-time evolution of strongly interacting matter remains a frontier of fundamental physics, as classical simulations are hampered by exponential Hilbert space growth and rapid, unmanageable growth of quantum entanglement. This study reports the quantum simulation of hadron dynamics within a $(1 + 1)$ -dimensional $SU(2)$ lattice gauge theory using a 156-qubit IBM superconducting processor. Leveraging a hardware-efficient Loop-String-Hadron (LSH) encoding, we simulate the dynamics of the physical degrees of freedom on a 60-site lattice in the weak-coupling regime, as a crucial step toward the continuum limit. We successfully observe the light-cone propagation of a confined meson and internal oscillations indicative of early-time hadronic breathing modes. Notably, these high-fidelity results were obtained directly from the quantum data via a differential measurement protocol, together with measurement error mitigation, demonstrating a robust pathway for large-scale simulations even on noisy hardware. To validate the results, we benchmarked the quantum algorithm and its outcomes from the quantum processor against state-of-the-art approximated classical algorithms using tensor network methods and Pauli propagation, respectively. Furthermore, we provide a quantitative comparison demonstrating that as the system approaches the weak-coupling or the continuum limit, the quantum processor maintains a consistent structural robustness where classical tensor networks and Pauli propagation methods encounter an onset of exponential complexity or symmetry violations as an artifact of approximation in the algorithm. These results establish a scalable pathway for simulating non-Abelian dynamics on near-term quantum hardware and mark a critical step toward achieving a practical quantum advantage in high-energy physics.

While Euclidean Monte Carlo methods successfully compute static properties, they cannot tackle real-time evolution due to the sign problem. Tensor Network (TN) methods offer a partial solution in low dimensions but hit a fundamental “entanglement wall” during quenches: as time evolves, the entanglement entropy $S(t)$ grows linearly, requiring the bond dimension to grow exponentially to maintain accuracy. This renders long-time simulations of large lattices computationally prohibitive for classical machines.

Quantum simulation, utilizing either digital gate-based or analog approaches, provides a fundamental route around this barrier by mapping gauge fields directly onto controllable quantum degrees of freedom. However, scalable experimental demonstrations have been predominantly confined to Abelian models, such as $U(1)$ or \mathbb{Z}_2 lattice gauge theories [1, 2, 3, 4, 5, 6, 7, 8, 9, 10, 11, 12, 13, 14, 15]. The transition to non-Abelian symmetries [16, 17, 18, 19, 20, 21, 22, 23], a strictly necessary step for simulating $SU(3)$ and the phenomenology of Quantum Chromodynamics (QCD) [24, 25], remains stalled by the difficulty of enforcing non-commuting Gauss’s laws on physical hardware. While analog simulators often lack the flexibility to implement these complex local constraints, current digital quantum devices face a parallel challenge: the deep circuits required to enforce gauge invariance are typically overwhelmed by hardware noise. Accessing the dynamics over longer timescales and reaching the continuum, or even the thermodynamic limit, remained a long-term goal for the community.

In this work, we overcome these limitations by using the Loop-String-Hadron (LSH) framework [26], which restructures the local Hilbert space to enforce Gauss’s law without the non-local string operators that plague standard Jordan-Wigner encodings. With this hardware-efficient encoding approach, we are able to scale the simulation of the dynamics of a meson in $(1 + 1)$ -dimensional lattice gauge theory to a 60-staggered-site $SU(2)$ model using a 156-qubit superconducting processor—approaching the thermodynamic limit. The coupling constants are chosen to fall in the weak-coupling regime, where entanglement is expected to grow rapidly, while the quantum algorithm involves a constant circuit depth per time step. We simulate dynamics of the system with a noise-resilient measurement protocol [27]. By isolating the coherent signal through differential observation, we extract high-fidelity hadronic physics directly from the data, reducing the gap between small-scale proofs of principle and utility-scale quantum hardware.

State-of-the-art classical simulation of the quantum circuit, the Pauli Propagation method [28] as well as tensor network simulation of the physical system are performed to validate the quantum algorithm and experimental results. A separation in time scaling is observed between the quantum execution time with a fixed shot budget and measurement error mitigation, and execution of classical algorithms, suggesting a possible algorithmic benefit in obtaining time evolution data over a small time win-

Gauge theories form the bedrock of the Standard Model, yet predicting their non-equilibrium dynamics remains notoriously dif-

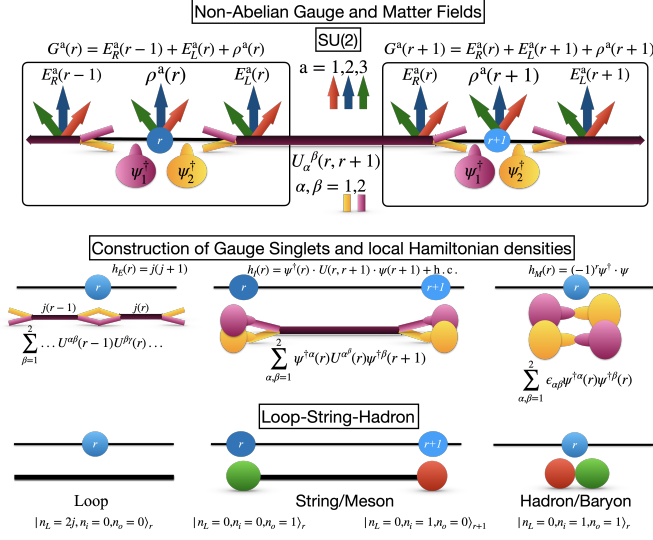


Fig. 1: From gauge redundancy to physicality: The local electric fields (E^a) and charge densities (ρ^a) of a non-Abelian gauge theory carry colour index, add up to form the Gauss law operator G^a and are elements of the Lie algebra with $a = 1, 2, 3$ for SU(2). The link operators and matter fields carry fundamental group index $\alpha = 1, 2$ at each site, which transform by the generators of the Lie algebra present locally. The physical states are defined to be gauge invariant, which are annihilated by the generators of the Lie algebra. At the top panel, we represent the variable of SU(2) gauge theory with open arms, corresponding to their adjoint and fundamental indices. In the middle panel, a cartoon representation of the gauge invariant objects is shown, represented by no open arms to any of the variables, with all the indices being contracted. For conventional gauge theory formulations, this construction involves forming the singlets, which are non-local for loops and strings, which are on-site for Baryons. The LSH framework directly maps these compound gauge singlets to LSH degrees of freedom and is presented in the bottom panel. A global physical state is represented by a direct product state in LSH basis, characterized by only integer quantum numbers $\prod_r |n_l, n_s, n_b\rangle_r$, and can be directly used as a computational basis.

dow. Probing deeper into the weak coupling domain revealed when both the tensor network and Pauli Propagation struggles with entanglement barrier and growth of non-clifford ness. The quantum processor, on the other hand is not affected by any of these except hardware noise in the current era of pre-fault tolerant hardware. A potential benefit can thus be envisioned in quantum simulating the strong interaction of nature with fault tolerant device and current work paves the pathway.

The Physics and the Experiment

In this work, we focus on the simplest continuous, yet non-Abelian, gauge group SU(2) in (1 + 1) spacetime dimensions with the ultimate aim of simulating the strong interactions of nature, described by SU(3) gauge theory in (3 + 1) dimensions. The system consists of dynamical fermions (matter) interacting via SU(2) gauge fields defined on the links of a spatial lattice. Understanding the structure and dynamics of entanglement entropy provides a new tool in the era of quantum information science [29]. Although various dynamical phenomena have been envisaged in different model-building and phenomenological pre-

dictions [30, 31], the scientific community has been waiting for an ab initio calculation or a quantum simulation demonstrating its validity and revealing many quantum mechanisms underlying the existing effective or microscopic description of physics in out-of-equilibrium or in extreme environments.

The Hamiltonian and Its Continuum Limit

The dynamics of gauge fields coupled with staggered fermions are governed by the Kogut-Susskind Hamiltonian [32]. The Hamiltonian contains an electric energy term (H_E), a staggered mass term H_M and a matter gauge interaction term (H_I) combined as:

$$H = \frac{g^2}{2a} H_E + m H_M + \frac{1}{2a} H_I \quad (1)$$

The parameters g , m , and a denote the gauge coupling, lattice fermion mass, and lattice spacing, respectively. The central challenge in simulating high-energy physics is to recover the *continuum limit*, in which the lattice spacing $a \rightarrow 0$ and the discrete theory faithfully reproduces the continuous quantum field theory (QFT). In (1+1) dimensions, this limit corresponds to the regime of vanishing coupling, $g \rightarrow 0$, provided the simulation volume is sufficiently large to capture the relevant physics. The volume of the system is given by $L = Na$, for an N -site system. The Hamiltonian given in (1) can be scaled as

$$W = \frac{2a}{g^2} H = H_E + \mu H_M + x H_I \quad (2)$$

The couplings in W with electric, mass and matter-gauge interaction terms are dimensionless and given as 1, μ , x respectively, where $x = \frac{1}{g^2 a^2}$ & $\mu = 2 \frac{m}{g} \sqrt{x}$. For a chosen fixed value of $\frac{m}{g}$, the continuum limit of the theory lies at $N \rightarrow \infty$ and $x \rightarrow \infty$ [33]. The work primarily focuses on $N = 60$ and $x = 100$, where the results from tensor network and Pauli propagation methods agree reasonably with the QPU result, with the chosen level of accuracy, and demonstrate runtime advantage for QPU for a fixed shot budget with measurement error mitigation only. We further study a lower and a higher value of x , to conclude that the struggle for classical simulations using tensor network or Pauli Propagation Method increases with increasing value of x , keeping N constant. This is presented later in this article.

Encoding Non-Abelian Gauge Invariance

A crucial hurdle in simulating the dynamics of a gauge theory arises from the need for gauge invariance. Although a gauge-invariant and orthonormal basis provides a natural choice for efficient encoding, commonly used basis - such as Wilson loops and strings - are inherently non-local. A further difficulty lies in expressing the Hamiltonian in terms of universal gate sets implementable on physical quantum hardware. When dealing with noise in today's quantum hardware, locality can be crucial for maintaining gauge invariance throughout the dynamic simulation. To date, a scalable and immediately implementable algorithm for non-Abelian gauge theories has remained absent, even in the era of utility-scale quantum hardware [34].

The dynamics, governed by the Hamiltonian in (1), preserves gauge invariance generated by a set of three Gauss law operators $G^a(r)$ for $a = 1, 2, 3$ and $\forall r$. These generators satisfy the SU(2) algebra at each lattice site. The physical or gauge invariant states are defined to be annihilated by all the SU(2) Gauss's law constraints at all lattice sites. In literature, these gauge-invariant degrees of freedom are described by the non-local Wilson loops, strings, and hadrons (mesons and baryons). This work adopts

the loop-string-hadron (LSH) framework for SU(2) lattice gauge theory [26] as an efficient approach that addresses the challenges associated with a non-abelian gauge theory and non-local interactions.

The LSH framework is a reformulation of Kogut-Susskind's original framework [32], obtained via the prepotential formalism [35, 36, 37, 38]. The LSH basis states can be intuitively understood to be on-site snapshots of all possible non-local loops of electric fluxes, strings connecting a quark matter, and hadrons (baryons and mesons), denoted as $|n_l, n_i, n_o\rangle_r$, that can be present globally on the lattice as denoted in Fig. 1 and satisfy an Abelian Gauss Law (AGL) constraint on each link, ensuring the continuity of electric flux lines. The LSH Hamiltonian consists of the diagonal number operators and ladder operators for the local LSH degrees of freedom and satisfies all the AGLs.

The SU(2) LSH Hamiltonian in 1 + 1 dimension has been extensively analyzed in the context of developing efficient quantum algorithms for simulating this theory and it has shown to offer significant reduction in qubit costs and gate depth, for both near and far-term quantum hardware [39]. The Hamiltonian is expressed in terms of occupation number and ladder operator for the on-site LSH degrees of freedom.

In contrast, this work presents quantum simulation of LSH dynamics implemented on state-of-the-art 156-qubit IBM quantum processor. The aim of the work is to probe the continuum limit, which requires probing the dynamics in the weak-coupling regime $x \gg 1$ for a lattice of reasonably large size. In this parameter regime, (i) the dynamics is dominated by the off-diagonal term in (2). For an approximation performed for H_E , it affects the dynamics less significantly, as compared to the other coupling regime $x < 1$. (ii) Without any loss of generality, one may consider a lattice with open boundary conditions, where a large number of incoming fluxes just pass through the lattice keeping the global charge sector same as the strong coupling vacuum (SCV)¹. The contribution of this background fluxes can be approximated as a global phase in this regime. This weak coupling approximate version of the LSH Hamiltonian has previously been developed in the context of analog simulation [40]. The algorithm identifies certain fermionic configurations at a site ($n_i = 0, n_o = 1$), when a new flux is created on a link emerging from the lattice, and its electric energy contribution is counted to contribute.

Encoding and preparing the initial states

In a 1 + 1-dimensional lattice, electric flux loops can flow in only one direction, and at each site a fermionic doublet can exist. This translates to an on-site physical state at r to be characterized as $|n_l(r), n_i(r), n_o(r)\rangle$. As illustrated in Fig. 2, the manifestly gauge singlet quantum numbers, n_l , denotes the electric flux passing through the site without any change and can vary from zero to infinity; $n_i = 1$, denotes an incoming flux being absorbed at that site by an on-site fermion forming a string-end like object for an incoming string; $n_o = 1$, denotes an outgoing flux being created at that site by an on-site fermion forming a string-end like object for an outgoing string. Fermionic statistics restricts n_i, n_o to take values between (0, 1), while being bosonic, n_l can be any positive semi-definite integer. Abelian weaving across the neighbouring

¹ The symmetry of LSH Hamiltonian preserves the following global charges

(i) total Baryon number: $\mathcal{B} = \sum_{r=0}^{N-1} (n_i(r) + n_o(r)) - N$, and (ii) net lattice flux: $q = \sum_{r=0}^{N-1} (n_o(r) - n_i(r))$. This translate to conserving the global observables $q_o = \sum_{r=0}^{N-1} n_o(r)$ and $q_i = \sum_{r=0}^{N-1} n_i(r)$.

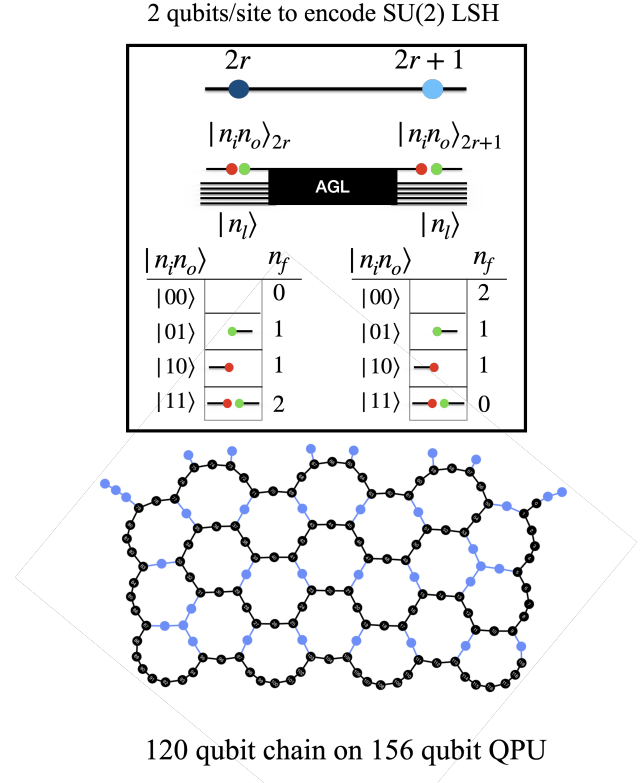


Fig. 2: Encoding physical degrees of freedom to qubits.

The local fermion number is defined on the staggered lattice as $n_f(r) = n_i(r) + n_o(r)$ for even sites and $n_f(r) = 2 - [n_i(r) + n_o(r)]$ for odd sites. At any site, $n_f = 2$ denotes the presence of a Baryon, $n_f = 1$ denotes the presence of the end of a meson or a longer string, and $n_f = 0$ denotes the vacuum for fermions. In the bottom panel, the qubit layout is given. Using the Qiskit Transpiler, the least noisy 120 qubit chain is obtained, which is denoted in black on the hardware layout. This allows one to perform a simulation for a 60-site lattice.

sites following the AGL is given by the on-link constraint

$$\text{Abelian Gauss Law : } n_l + n_o(1 - n_i) \Big|_r = n_l + n_i(1 - n_o) \Big|_{r+1} \quad (3)$$

As a consequence of the fact that gauge field are not dynamical for one spatial dimension, the quantum number n_l across the lattice is determined by the boundary flux and the fermion configurations throughout the lattice in order to satisfy the AGL at all the links of the lattice. This basis, being a strong coupling basis, yields the electric and mass part of the Hamiltonian H_E, H_M to be diagonal terms. While the off-diagonal terms of the Hamiltonian, the matter-gauge interaction H_I , cause the dynamics of loops, strings and hadrons on the lattice.

The initial state is chosen to be an unentangled state, which is a strong coupling eigenstate in LSH basis. A natural choice of such a state is the SCV, which corresponds to a ‘no particle - no antiparticle’ state with $n_f = 0$ at all sites. Next, a different initial state is prepared, where a meson is placed at the middle of the lattice, where $(n_f(r) = 1, r = N/2 - 1, N/2)$, while keeping $n_f = 0$, elsewhere as illustrated for a small lattice in Fig. 3.

Observing Real-time Dynamics

In this work, quench dynamics of a single hadron propagating through a dynamical medium are studied for a spatial lattice with

60-staggered sites and for 25-trotter steps. Towards this goal, first, the SCV is prepared and evolved for t_n Trotter steps. Next, the hadronic state is also evolved for the same number of Trotter steps. For both run, the state of the qubits are measured in σ_z basis and the probability for finding it up or down is calculated for a large number of copies of the same experiment. This is repeated for $t_n = 1, 2, 3, \dots, 25$. A schematic representation of the time evolution of such a quantum state is presented in Fig. 3.

The probability distribution obtained in the first experiment (the vacuum (SCV) fluctuation) is subtracted from the probability distribution of the time evolution of the hadron placed on the SCV. The experiment’s findings and their benchmarking are presented in the next section and in Fig. 4.

The experimental quantum simulation as well as classically simulated results reveal an early-time breathing mode of hadron, characterized by internal oscillations of cluster formation and decay [30] driven by the highly entangled environment. Extracting the same information from the tensor network calculation is straightforward and reveals an interesting observation towards hadronization of the universe as envisaged in [41, 42]. Continuing the evolution for longer would allow the hadron to reach its critical length for string breaking. String breaking would reduce entanglement. With further time evolution, the entire spatial lattice is expected to get hadronized, a state, with no/minimal long-range entanglement [31].

The experiment on QPU is performed with a circuit of more than 17000+ two-qubit gates and 90000+ single qubit gates, and a fixed 10,000 shot budget per trotter step. The depth of 2-qubit gates for simulating the Time evolution, grow up to 259 for 20, and to 324 for 25 Trotter steps respectively. Using only a low-cost readout error mitigation [27], the signal from QPU shows a coherent signal for propagation of a hadron by extending its size at each Trotter step, but confined within a ‘light-cone’. The edges of the ‘light cone’ trace a curved path instead of a straight line, denoting the constituent quarks to stay confined by the strong force instead of flying away freely.

The experimental observation is benchmarked by two classical computing methods: (i) Tensor Network (TN) calculations performed for the original LSH Hamiltonian and basis, via construction of Matrix Product Operators (MPO) and Matrix Product States (MPS) respectively, carefully created as a toolbox for LSH calculations [43]. The time evolution is computed using a 2-site TDVP algorithm that is free of Trotterization error. The bosonic cut-off for this computation is set at $2j_{max} = 5$, while a cut-off in bond dimension is set at $D_{max} = 200$. This method, albeit approximate, has been checked to provide acceptable convergence up to the time limit observed. (ii) A recently developed algorithm to classically simulate a quantum circuit, the Pauli Propagation Method (PPM) [28], is employed to simulate noiseless simulation of the circuit for 120 qubits. This method involves careful operator backpropagation via identifying the gate operations and qubits responsible for each measurement. The approximation of this method is due to the use of a finite number of Pauli terms in the operator expansion. The maximum of this number is calculated by extrapolating the exact number of Pauli terms for the circuit with lower gate depths (the first few Trotter steps) to minimise truncation error.

Fig. 4 compares the high-fidelity observables obtained from experimental observations, quantum simulation on *IBM Boston* with only measurement error mitigation, a tensor network calculation for the full LSH Hamiltonian, and a classical simulation of the quantum circuit via the Pauli propagation method. While the heatmaps for the first two agree visually, both for the over-

all light-cone nature and the internal structure of the hadrons at any time slice, further investigation yields quantitative agreement between the high-fidelity results obtained using the TN and PP methods (performed on GPU and presented in Fig. 5), suggesting that the approximations made in the original theory to produce an implementable circuit are valid. Noiseless simulation of a quantum circuit is obtained via PP, and comparing the same to the experimental results demonstrates the effect of noise as depicted in the non-zero background beyond the lightcone for QPU data in Fig. 4, and the damped signal in n_f values in Fig. 5). However, without active error mitigation (only with measurement error mitigation), the experimental outcomes of observables remain largely noise-resilient in the pre-fault-tolerant era. We use two different approximation strategies for PP: truncation to a maximum number of terms and truncation based on a minimum coefficient cut-off ($< 10^{-5}$) for each Pauli term, on CPU and GPU, respectively.

While the exact dynamical values of the observables remain unknown for the system size under consideration, we quantify errors in the particle-density observable $n_f(t) = \sum_{r=1}^{60} n_f(r, t)$ by combining (i) inter-method spread and (ii) violation of the exact global constraint ² and is reported in Fig. 5.

Fig. 4 and Fig. 5 together validate the experimental observation’s resilience to noise, along with the validity of the weak coupling approximation and the associated quantum algorithm. Comparison of the time taken for each Trotter step using classical and quantum algorithms shows a clear separation in scale, and the same holds for a complete simulation of dynamics up to a fixed time, while the error bars for classical and quantum implementations remain comparable. The tensor network experiment on classical computing hardware encounters an entanglement wall. The time complexity grows exponentially with the entanglement entropy. Ideally, it requires increasing the value of the allowed maximum bond dimension D_{max} to minimise the error. In this work, D_{max} was limited to 200 due to constraints on available computing resources. With this particular limit on D_{max} , the dynamics beyond 20 Trotter steps are obtained to contain errors which can not be neglected and hence is not reported. The details are reported as supplementary information. In summary, TN calculations are not found to be useful for computing dynamics for longer times as the coupling $x \rightarrow \infty$ with finite computing resources. The quantum simulation continues to perform effortlessly in the high-entanglement regime and demonstrates coherence. Invading long-time dynamics for $x \rightarrow \infty$ is not a challenge for a quantum computer except for the loss of coherence due to noise. The reported dynamics of the observable depict noise resilience, with the differential measurement protocol employed in this experiment. The compute time on the QPU is 20 seconds per time step and depends primarily on the number of shots. For our experiments, we have used a fixed budget of 10,000 shots. The Pauli propagation method [28] provides an efficient classical algorithm for simulating an error-free quantum circuit. This method is employed on CPU, with an estimate of max-term obtained via extrapolations of exact results for small-sized systems to minimise truncation error. The simulation time of PP *on a CPU* grows linearly with the number of trotter steps. We further employ another strategy with PP *on GPU*, where the terms with a coefficient greater than a threshold are considered. The error bars obtained with this approach are comparatively smaller than those obtained with the other approach; however,

²Globally conserved charges as per 1 are exactly known. For the chosen initial states, these should take the value $Q = 60, q = 0$ throughout the dynamics. The observable $n_f(r, t)$ is directly related to on-site contribution to the global charge Q .

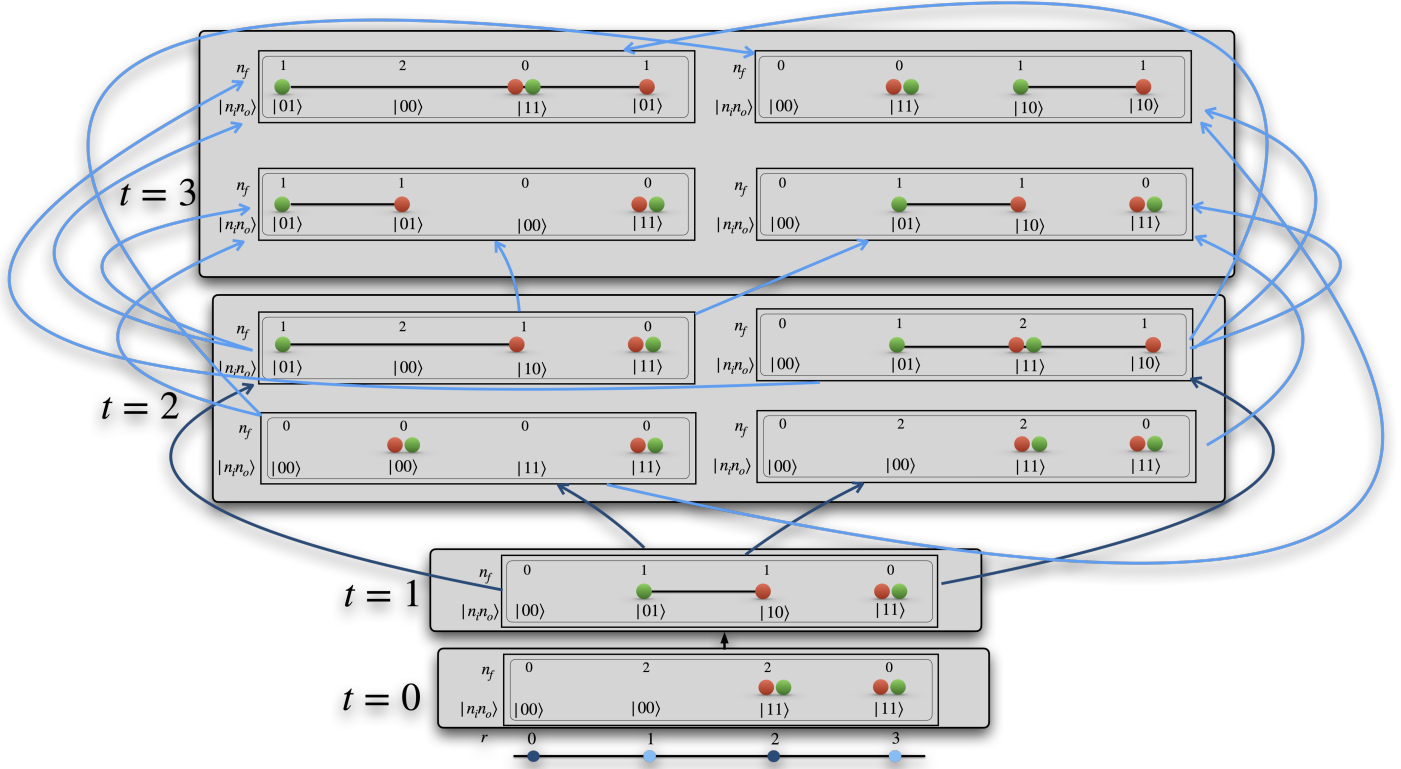


Fig. 3: Schematic of quantum evolution on a 4-site lattice. The diagram illustrates the buildup of entanglement and particle number fluctuations over 3 Trotter steps under the LSH Hamiltonian. The system is initialized at $t = 0$ in a zero-entanglement product state containing two baryons (total fermion number $n_f = 4$). At $t = 1$, the evolution transitions the system to a single meson state ($n_f = 2$). Subsequent steps ($t = 2, 3$) generate increasingly complex superpositions of states with varying particle numbers ($n_f \in \{2, 4, 6\}$), governed by the interplay of the electric (H_E) and mass (H_M) Hamiltonian terms. This fluctuation of total particle number is a hallmark of relativistic quantum field theory. Each basis state is represented as $\otimes_r |n_i, n_o\rangle_r$ and mapped directly to qubit registers. The values of $n_f(r, t)$ across the lattice at all time steps are measured to construct the experimental heatmaps presented in this work. The branching of the wavefunction depicted here highlights the rapid growth of entanglement, rendering the full 120-qubit simulation classically intractable.

the time scaling no longer remains linear, even with parallelisation on a GPU.

In summary, the Pauli propagation method works efficiently for a circuit with high entanglement but low magic (the non-stabilizer resource required to achieve a computational advantage over classical systems, refers to states or operations that cannot be simulated by classical computers using only stabilizer circuits and Clifford operations). While the quantum algorithm involved in this particular simulation not only causes a growth of entanglement entropy via its two-qubit gate operations (as extracted from the tensor network calculations), it also contains a significant amount of non-Clifford gate operations.

The quantum simulation protocol is further tested for a couple of different values of coupling $x \rightarrow x/2$ and $x \rightarrow 2x$, without changing the value of m/g . The experimental observation confirms the expected ‘shrinking’ and ‘widening’ of light cone structure in Hadron propagation respectively as shown in Supplemental material, confirming the robustness of the algorithm, implementable on QPU. Classical benchmarking, TN simulation for the complete LSH Hamiltonian and the noiseless simulation of the quantum circuit with PP, are also performed for $x = 50, 200$. The results are summarized in Fig. 6. Despite being a circuit with the same gate depth, the classical simulation for $x = 50, 100, 200$ experienced increased time complexity, suggesting the growth of non-Clifford operations as the continuum limit of the theory is

approached. Tensor network calculation, worked almost flawlessly for $x = 50$, struggled beyond 20 Trotter steps for $x = 100$, and almost completely broke down for $x = 200$ after 10th Trotter steps, as evident in the entanglement dynamics captured by the TN calculation and presented in Fig. 6. The PP started violating global symmetries at $x = 100, 200$, whereas it remained robust at $x = 50$. In summary, classical algorithms, when based on a tensor network, face the entanglement wall, whereas a classical simulation of a quantum circuit is limited by the circuit’s magic. Quantum processors have limitations arising from noise, not from entanglement or magic, and thereby provide an alternative pathway to perform these computations in the fault-tolerant era. The observed classical bottlenecks are not merely incidental failures of two approximate algorithms, but are consistent with the intrinsic ergodic and chaotic structure of the same gauge theory Hamiltonian in the relevant parameter regime [44].

Outlook

The current work paves the way for performing ab initio calculations in Quantum Chromodynamics using a quantum computer, and demonstrates that scalable quantum simulations of non-Abelian gauge theories are feasible even in the pre-fault-tolerant era, beyond proof-of-concept experiments.

By successfully accessing a 60-site lattice, the current work es-

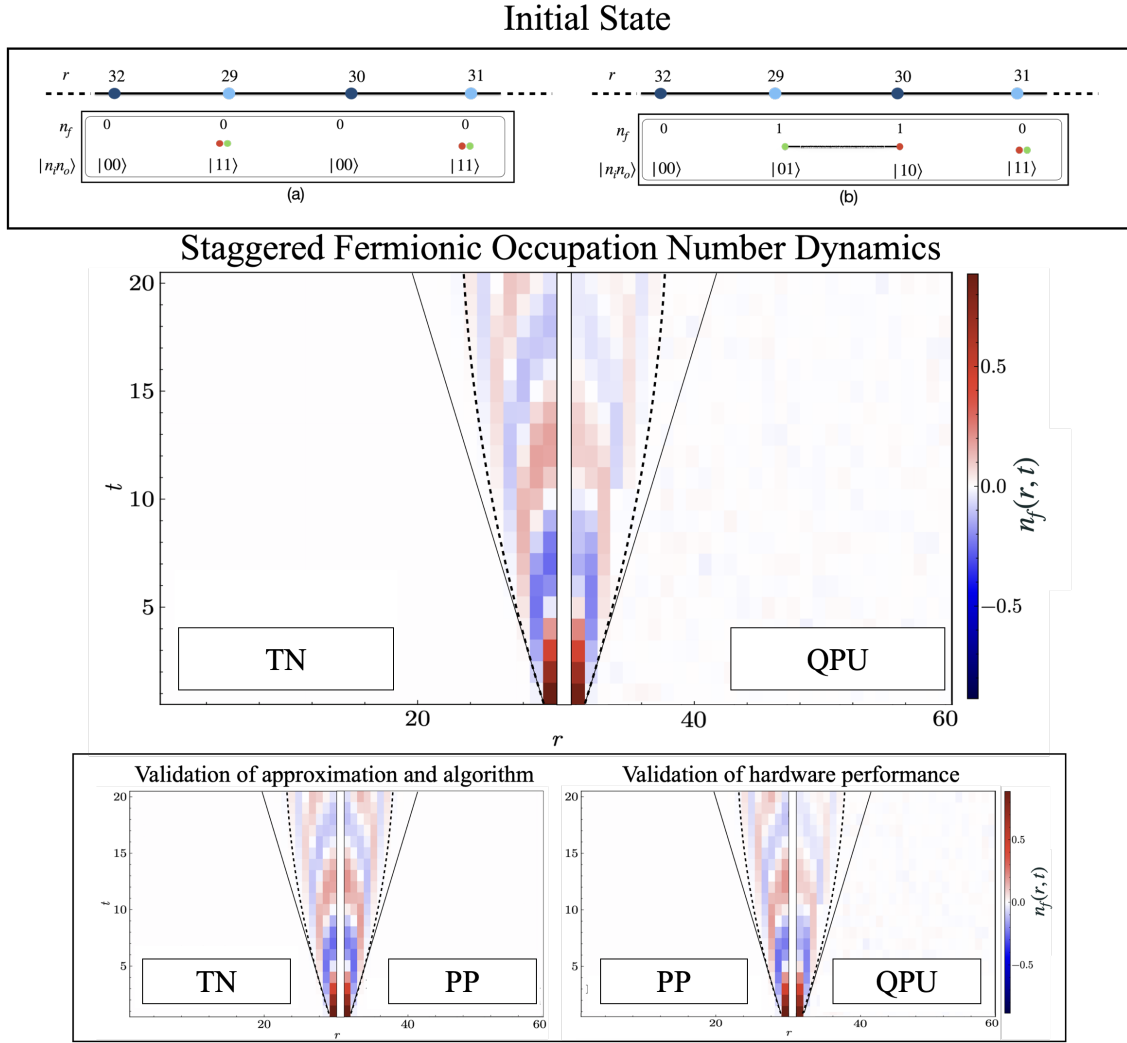


Fig. 4: Real Time Propagation of SU(2) Hadron: validation of the ansatz, algorithm, and hardware implementation. The top panel displays a cartoon representation of the initial states; (a) The SCV for a staggered lattice, and (b) A meson is placed at the middle of the lattice on top of the SCV. The fermion/antifermion number $n_f = 0$ at all sites except at two middle sites of (b), which are both singly occupied and are characterized by $n_f = 1$. The lower panels show the light-cone (t vs lattice site r) propagation of a meson placed at the centre of the lattice at $t = 0$, here t denotes the dimensionless time after each Trotter step. The site-resolved fermion number $n_f(r, t)$ for the time evolution of the state (b) subtracted from the same for initial state (a), is plotted for 20 time steps. Space-time evolution of particle density n_f on a 60-site lattice is compared using three different approaches: (i) QPU: Quantum simulation on *IBM Boston* using only measurement error mitigation; (ii) TN: Tensor network calculation using the MPS and MPO constructed for the full LSH Hamiltonian with a maximum bond-dimension of 200. (iii) PP: Pauli Propagation method applied for the classical simulation of the quantum circuit with a truncation in the maximum number of allowed terms in the operator expansion. The dynamics on the left half of the figure (lattice sites 0 – 29) are from one calculation, while the right half of the plot shows another. The clear agreement between the left and right halves of the heat map in the middle panel confirms the validity of the experimental result as a simulation of the exact theory. The TN calculation is performed for the full LSH Hamiltonian, and the algorithm (TDVP) doesn't involve Trotterization error. The Quantum simulation is performed using the weak-coupling approximated LSH and first-order Trotterization. The visible match between the left and right sides in the middle panel validates both approximations in the experimental observation. The pair of curved dotted lines in each plot is added to guide the eye to the confined structure of the meson, in contrast to the solid straight lines drawn with the initial slope of the propagation. The internal oscillation of red and blue pixels correspond to the early time breathing mode of hadrons. In the bottom panel, the visible match for TN and PP provides a stronger validation of the ansatz, while the mismatch between PP and QPU suggests the effect of hardware noise in experimental observation.

establishes that pre-fault-tolerant hardware, when combined with hardware-efficient encodings such as LSH and error-robust measurement protocols, can capture non-perturbative dynamics inaccessible to classical methods. This success opens several distinct avenues for future research.

First, extending the simulation time beyond the current window is an immediate priority. Our results hint at the early stages of hadron breathing and entanglement growth; prolonging the evolution would allow for the direct observation of string breaking and the subsequent hadronization of the vacuum—phenomena

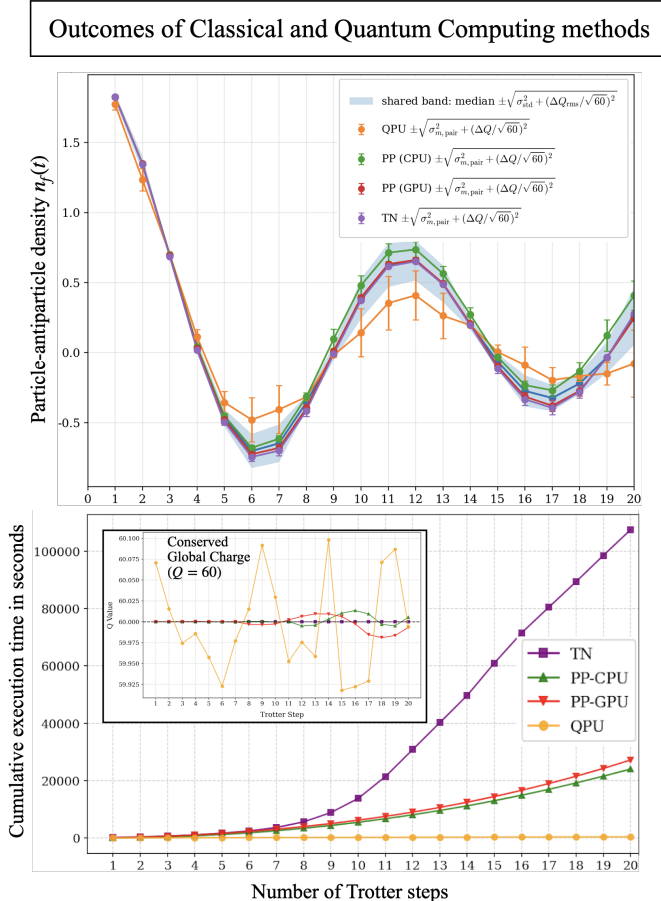


Fig. 5: Error bound vs. compute time for observable corresponding to average particle-antiparticle density $n_f(t) = \sum_r n_f(r, t)$. We consider four independent computed value of the observable $n_f^{(m)}(t)$, $m \in \{\text{TN}, \text{PP - CPU}, \text{PP - GPU}, \text{QPU}\}$. For these distributions, the median is used as the reference point, and the intrinsic method-to-method uncertainty is taken as the sample standard deviation. Independently, global-symmetry conservation through the total charge $\mathcal{B} + N = Q (= 60)$ is monitored (inset of the bottom panel), and its per-site contribution is added to get a final shared uncertainty band (shown as a shaded region, in the top panel). It captures both cross-method variability and global-constraint inconsistency. Additionally, for each method, we report individual error bars reflecting deviations from the median. The cumulative computation time for each method is also presented in the bottom panel. The data reveals that the TN method to be the most time-consuming, but with the smallest error bar. PP-CPU is performed based on a guess of the maximum number of allowed terms. The computation time scales much better with TN, but the error bars are larger. The same PP algorithm is implemented on a GPU, along with a definite truncation scheme for the Pauli-term coefficients, yielding results with smaller error bars but the compute time scales faster. The result from the QPU follows the distribution pretty well, with error bars that enter the shaded region at all time slices, yet it performs the computation in much less time (400 seconds to complete 20 Trotter steps).

that are central to understanding the thermalization of the quark-gluon plasma formed in heavy-ion collisions [41, 31, 30].

Second, the LSH framework utilized here is naturally extensible to higher dimensions and more complex gauge groups. The most significant barrier to simulating Quantum Chromodynamics (QCD) has been implementing the SU(3) gauge group. The methods validated in this work for SU(2) provide a blueprint for advantage in encoding SU(3) gauge theory to qubits via LSH framework built upon the prepotential formulation [45]. The 1+1-dimensional framework is ready to use [46], while the higher-dimensional framework is being developed step by step [47, 48].

Finally, the efficient encoding and the error-resilient differential observation technique used in this work, and confirmation of its validity in capturing correct physical dynamic establishes a pathway for computing novel real-time dynamics with quantum advantage [49]. We demonstrate that our differential measurement protocol effectively isolates the coherent physical signal without the need for active error mitigation. As hardware fidelity continues to improve, along with appropriate active error mitigation or early error-correction protocols, these methods are expected to enable increasingly sophisticated simulations of scattering phenomena. When applied to finite-density systems where the Monte Carlo sign problem is most severe, could soon unravel the phase diagram of dense nuclear matter, shedding light on the interiors of neutron stars and the early universe. The observation of the dynamical evolution of the entanglement entropy in Fig. 6, obtained via tensor network calculation, reveals the signature of the pre-Hadronisation phase (hadron passing through a highly entangled region) of the universe probed within the time scale reported. Allowing the dynamics to run longer and with a larger number of probes may enable the simulation of hadronisation in the early universe. Furthermore, the enhancement of this work can lead to the ability to study collisions of mesons and baryons and to probe parton distribution functions and deep-inelastic scattering processes from first principles would mark a substantial expansion in the range of non-equilibrium quantum field theory calculations accessible to computation, extending beyond what is currently practical with classical lattice QCD techniques.

Data Availability

The data supporting the findings of this study are available at the public [GitHub](#) repository.

Code Availability

The codes used for the findings of this study are available from the corresponding author upon reasonable request.

Acknowledgments

The authors would like to thank Abhinav Kandala and Nick Bronn for insightful discussions and feedback at various points of this work and for sharing comments on the manuscript. We would also like to thank Rudranil Basu for discussion and help in GPU implementation of the Pauli propagation method. IR would like to thank Jesse Stryker, Zohreh Davoudi, Saurabh Kadam, Navya Gupta, and Aahiri Naskar for their continuous contributions in developing the loop-string-hadron framework and for numerous discussions during all collaboration meetings. The work reported here is performed using the IBM Quantum Credits received by

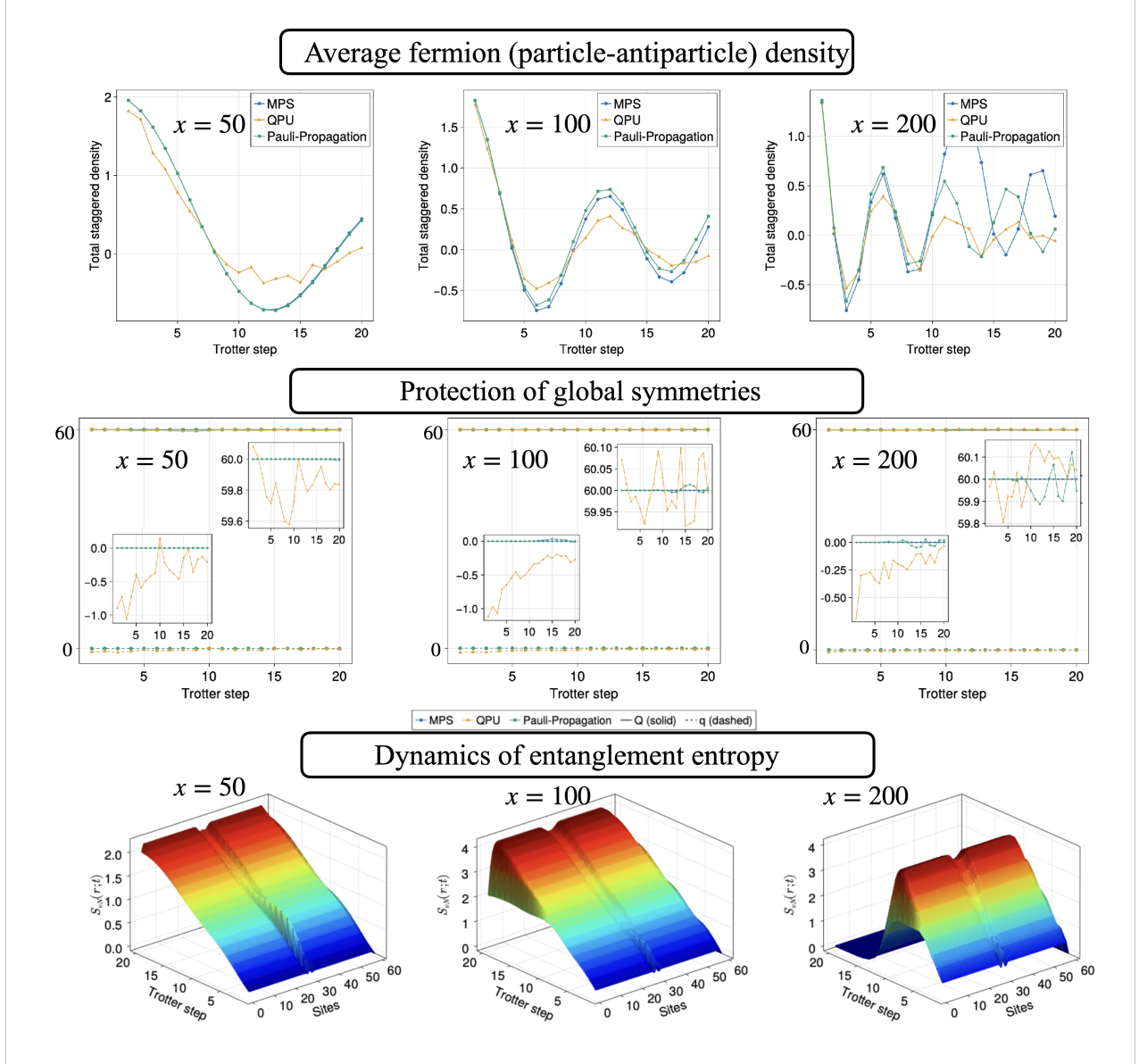


Fig. 6: Comparing robustness of quantum simulation versus classical simulation towards $x \rightarrow \infty$. Top row: The dynamics of average fermion density is plotted with time. For $x = 50$, MPS and PP agree exactly, QPU shows deviation but follow the trend. For $x = 100$, MPS and PP start to separate out after 5th Trotter steps, QPU deviates but follows the trend. For $x = 200$, post 10th Trotter step, MPS and PP do not follow the same trend, QPU follows PP, with deviation. Middle row: The conservation of global charges are tracked for all simulation. Overall it stays conserved in all the methods. As presented in the insets, QPU shows a small deviation, for all x values. MPS preserves the global constraints by construction [43]. PP shows small deviation, and it increases with increasing x . Bottom row: The entanglement entropy, obtained via TN calculation, shows linear growth for $x = 50$, saturates to a plateau for $x = 100$, while the allowed bond dimension fails to handle entanglement growth for $x = 200$ case, and in effect the MPS simulation fails to capture physics anymore. The drop in entanglement is an artifact of finite bond dimension, rather than being a physical phenomenon.

IR. The authors acknowledge the support. IR acknowledges useful discussions during meetings of QC4HEP working group. Research of IR is supported by the OPERA award (FR/SCM/11-Dec-2020/PHY) from BITS-Pilani and the cross-discipline research fund (C1/23/185) from BITS-Pilani. FI is supported by the cross-discipline research fund (C1/23/185) from BITS-Pilani. MdOA acknowledges computational and other support from BITS Pilani through another cross-discipline research fund (C2/24/282) from BITS-Pilani.

Authors' contributions

FI developed the quantum algorithm and benchmarked it against exact diagonalization, prepared the POC, performed noiseless classical simulation of the quantum algorithm.

RM helped design and map the quantum circuit tailored to the hardware, and ran all the quantum experiments, and performed noiseless classical simulation of the quantum algorithm.

EM performed the tensor network calculations to benchmark the performance of QPU, making all the plots and analyzing data.

MdOA set up the code in CUDA and performed the classical simulation using GPU.

NE helped analyze the quantum circuits and experimental results & evaluation, and contributed to manuscript preparation.

IR developed the problem statement, set up the algorithmic strategy, analyzed data, prepared the main manuscript, including graphics.

Competing interests

The authors declare no competing interests.

Methods

The theory to be simulated

In this section, we briefly review the theory we aim to simulate, the Kogut-Susskind Hamiltonian formalism, represented in the loop-string-hadron basis. As discussed in the main text, the continuum limit weak-coupling regime of the theory, encoded in the gates of the current experiment.

Kogut-Susskind Hamiltonian

The scaled Kogut-Susskind (KS) Hamiltonian describing SU(2) Yang Mills theory coupled to staggered fermions on (1+1)-d (1d spatial lattice and continuous time) [32] can be written as:

$$W = H_E^{(KS)} + \mu H_M + x H_I^{(KS)}. \quad (4)$$

The gauge link $U(r)$ is a 2×2 unitary matrix defined on the link connecting sites r and $r + 1$. A temporal gauge is chosen to derive the above Hamiltonian, which sets the gauge link along the temporal direction equal to unity. The color electric fields $E_{L/R}^a$ are defined at the left L and right R sides of each link, and they satisfy the following commutation relations (SU(2) algebra) at each end:

$$\begin{aligned} [E_L^a(r), E_L^b(r')] &= i\epsilon^{abc}\delta_{rr'}E_L^c(r), \\ [E_R^a(r), E_R^b(r')] &= i\epsilon^{abc}\delta_{rr'}E_R^c(r'), \\ [E_L^a(r), E_R^b(r')] &= 0, \end{aligned} \quad (5)$$

where ϵ^{abc} is the Levi-Civita symbol. The electric fields and the gauge link satisfy the following quantization conditions at each site,

$$\begin{aligned} [E_L^a(r), U(r')] &= -\frac{\sigma^a}{2}\delta_{rr'}U(r), \\ [E_R^a(r), U(r')] &= U(r)\delta_{rr'}\frac{\sigma^a}{2}, \end{aligned} \quad (6)$$

where σ^a are the Pauli matrices. For a theory including matter fields, staggered fermionic fields $\psi^{\dagger\alpha}(r)$, for $\alpha = 1, 2$ are present at each lattice site. The Hamiltonian in (4) is gauge invariant as it commutes with the Gauss' law operator,

$$G^a(r) = E_L^a(r) + E_R^a(r-1) + \psi^\dagger(r)\frac{\sigma^a}{2}\psi(r) \quad (7)$$

at each site r . The physical sector of the Hilbert space corresponds to the space consisting of states annihilated by (7). Solving the non-Abelian Gauss laws at each site r as given in (7) is non-trivial, and engineering the same in an experiment is the most difficult job.

LSH Hamiltonian

LSH formalism of lattice gauge theory is based on prepotential framework, where, the original canonical conjugate variables of the theory, i.e color electric field and link operators are replaced by a set of harmonic oscillator doublets, defined at each end of a link [35, 36, 50, 51, 52, 37, 45, 53, 38]. In prepotential framework, the SU(2) gauge group is confined to each lattice site allowing one to have local gauge invariant operators and states at each site, leading to a description of local loop segments. Combining prepotentials with staggered fermionic matter fields at each lattice site to form gauge invariant singlets, yields on-site string-end operators. Staggered matter fields also combine

into local gauge-invariant configurations representing hadrons, likewise in the original understanding of the theory. Thus the gauge invariant and orthonormal LSH basis is characterized by a set of three integers $n_l(r), n_i(r), n_o(r)$, corresponding to the loop, incoming string, and outgoing string at each site (on-site hadron is equivalent to simultaneous presence of both the string ends). LSH basis states satisfy all the Gauss' law constraints by the construction. The allowed values of the LSH quantum numbers are

$$0 \leq n_l(r) \leq \infty, \quad 0 \leq n_i(r) \leq 1, \quad 0 \leq n_o(r) \leq 1, \quad (8)$$

denoting n_l to be a bosonic excitation, whereas n_i, n_o to be fermionic in nature, even though the string ends contain information of both gauge field and matter content.

A set of LSH operators consisting of both diagonal and ladder operators are defined locally at each site as:

$$\hat{n}_{l/i/o}|n_l, n_i, n_o\rangle = n_{l/i/o}|n_l, n_i, n_o\rangle \quad (9)$$

$$\hat{\lambda}^\pm |n_l, n_i, n_o\rangle = |n_l \pm 1, n_i, n_o\rangle \quad (10)$$

$$\hat{\chi}_{i/o}^+ |n_l, n_i, n_o\rangle = (1 - \delta_{n_{i/o}, 1})|n_l, n_{i/o} + 1, n_{o/i}\rangle \quad (11)$$

$$\hat{\chi}_{i/o}^- |n_l, n_i, n_o\rangle = (1 - \delta_{n_{i/o}, 0})|n_l, n_{i/o} - 1, n_{o/i}\rangle \quad (12)$$

The LSH basis states must satisfy the AGL, as explained in the main text to be counted as a valid loop-string-hadron segment of the global loop configurations present on the lattice.

Hamiltonian of the theory,

$$W^{(\text{LSH})} = H_E^{(\text{LSH})} + \mu H_M^{(\text{LSH})} + x H_I^{(\text{LSH})} \quad (13)$$

is exactly equivalent to the original Hamiltonian (4), with the following form of electric term, mass term and matter-gauge interaction term in terms of LSH operators:

$$H_E^{(\text{LSH})} = \sum_{r=0}^{N-2} \left[\frac{\hat{n}_l(r) + \hat{n}_o(r)(1 - \hat{n}_i(r))}{2}, \right. \\ \left. \times \left(\frac{\hat{n}_l(r) + \hat{n}_o(r)(1 - \hat{n}_i(r))}{2} + 1 \right) \right] \quad (14)$$

$$H_M^{(\text{LSH})} = \sum_{r=0}^{N-1} (-1)^r (\hat{n}_i(r) + \hat{n}_o(r)), \quad (15)$$

$$H_I^{(\text{LSH})} = \sum_{r=0}^{N-1} \frac{1}{\sqrt{\hat{n}_l(r) + \hat{n}_o(r)(1 - \hat{n}_i(r)) + 1}} \times \quad (16) \\ \left[S_o^{++}(r) S_i^{+-}(r+1) + S_o^{--}(r) S_i^{-+}(r+1) \right. \\ \left. + S_o^{+-}(r) S_i^{-+}(r+1) + S_o^{-+}(r) S_i^{++}(r+1) \right] \\ \times \frac{1}{\sqrt{\hat{n}_l(r+1) + \hat{n}_i(r+1)(1 - \hat{n}_o(r+1)) + 1}}.$$

Here (16) contains LSH ladder operators in the following combinations (suppressing the explicit site index),

$$S_o^{++} = \hat{\chi}_o^+ (\hat{\lambda}^+)^{\hat{n}_i} \sqrt{\hat{n}_l + 2 - \hat{n}_i} \quad (17)$$

$$S_o^{--} = \hat{\chi}_o^- (\hat{\lambda}^-)^{\hat{n}_i} \sqrt{\hat{n}_l + 2(1 - \hat{n}_i)} \quad (18)$$

$$S_o^{+-} = \hat{\chi}_i^+ (\hat{\lambda}^-)^{1 - \hat{n}_o} \sqrt{\hat{n}_l + 2\hat{n}_o} \quad (19)$$

$$S_o^{-+} = \hat{\chi}_i^- (\hat{\lambda}^+)^{1 - \hat{n}_o} \sqrt{\hat{n}_l + 1 + \hat{n}_o} \quad (20)$$

and

$$S_i^{+-} = \hat{\chi}_o^- (\hat{\lambda}^+)^{1 - \hat{n}_i} \sqrt{\hat{n}_l + 1 + \hat{n}_i} \quad (21)$$

$$S_i^{-+} = \hat{\chi}_o^+ (\hat{\lambda}^-)^{1 - \hat{n}_i} \sqrt{\hat{n}_l + 2\hat{n}_i} \quad (22)$$

$$S_i^{--} = \hat{\chi}_i^- (\hat{\lambda}^-)^{\hat{n}_o} \sqrt{\hat{n}_l + 2(1 - \hat{n}_o)} \quad (23)$$

$$S_i^{++} = \hat{\chi}_i^+ (\hat{\lambda}^+)^{\hat{n}_o} \sqrt{\hat{n}_l + 2 - \hat{n}_o}. \quad (24)$$

The strong coupling ($x \gg 1, m/g = \text{fixed}$) vacuum of the LSH Hamiltonian is given by:

$$\begin{aligned} n_l(r) &= 0 \quad \forall r \\ n_i(r) &= 1, \quad n_o(r) = 1 \quad \text{for } r \text{ odd} \\ n_i(r) &= 0, \quad n_o(r) = 0 \quad \text{for } r \text{ even} \end{aligned} \quad (25)$$

which satisfy AGL on all the links. The spectrum and dynamics of the LSH Hamiltonian is obtained identical to the gauge invariant dynamics of the Kogut susskind Hamiltonian with the same value of bosonic cut-off using exact diagonalization [54]. The tensor network calculations reported in this work are based on the LSH framework and uses a bosonic cut-off $j_{max} = 5/2$, using the tensor network toolbox [43].

Approximations for weak coupling regime

We focus on open boundary condition, and allow an incoming flux l_i to enter the lattice. Towards the weak coupling domain, the interacting vacuum is not dominated by a zero-flux state, SCV, rather it is expected to contain all possible flux states as the electric energy contribution is significantly low, compared to the interaction energy. This allows us to choose $l_i \gg 0$, without any loss of generality [40]. Using AGL on each link, the value of n_l at each site can be fully determined as

$$\begin{aligned} n_l(r) &= l_i - n_i(r)(1 - n_o(r)) + \sum_{r'=0}^{r-1} (n_o(r') - n_i(r')) \\ &\approx l_i - n_i(r)(1 - n_o(r)) \quad \text{for } l_i \gg 0. \end{aligned}$$

Thus, any physical state in the LSH formalism in one spatial dimension is completely determined by (n_i, n_o) quantum numbers at each site, and the interaction can be approximated to be local. This approximation is valid [40] if we focus on the weak coupling regime $x \gg 1$, and the off-diagonals contribute more to the dynamics. Choosing the global charge sector same as that of the SCV i.e. with no net Baryon number and no net lattice flux $(\mathcal{B}, q) = (0, 0)$ (see the footnote 1), the minimum energy strong coupling configuration of the string-ends still remain the same as the SCV.

We further make an approximation of

$$\frac{n_l}{n_l + 1} \rightarrow 1 \quad \& \quad \frac{n_l + 1}{n_l + 2} \rightarrow 1$$

for all the prefactors appearing in H_I^{LSH} considering the $l_i \gg 1$ scenario.

Within this approximation, the total electric part of the LSH Hamiltonian is given by:

$$H_E^{(\text{approx})} = \frac{g^2 a}{2} \left[N h_E^0 + \sum_{\{r'\}} \left(\frac{l_i}{2} + \frac{3}{4} \right) \right] \quad (26)$$

where, $\{r'\}$ denotes the sites with fermionic configuration $n_i(r') = 0, n_o(r') = 1$ and h_E^0 , corresponds to a global phase due to the background flux.

Mass Hamiltonian: The mass term (15), being independent of gauge field configuration remain the same in the weak coupling approximation.

$$H_M^{(\text{approx})} = \sum_r (-1)^j (\hat{n}_i(r) + \hat{n}_o(r)) \quad (27)$$

Interaction Hamiltonian: The matter-gauge field interaction term is the most complicated within the LSH framework,

as detailed in (16). In the strong coupling limit of the theory, this particular term gives small contribution to the Hamiltonian. However, in the weak coupling regime of interest, this term becomes significant. The approximation scheme that we follow casts the interaction Hamiltonian given in (16) as,

$$H_i^{\text{(approx)}} = \sum_r \left[\chi_o^+(r)\chi_o^-(r+1) + \chi_o^+(r+1)\chi_o^-(r) + \chi_i^+(r)\chi_i^-(r+1) + \chi_i^+(r+1)\chi_i^-(r) \right] \quad (28)$$

The purpose of the present approximation scheme is to bring the interaction Hamiltonian into simple form, yet describing matter gauge dynamics in the weak coupling regime reliably.

In the next section, we present the quantum algorithm construction, starting with the mapping of LSH quantum numbers to the hardware's qubits and mapping the time evolution unitary for the weak coupling approximated Hamiltonian to a quantum circuit.

Algorithm for QPU

In this work we study the time evolution of the system for a scaled time τ for the scaled Hamiltonian W caused by the unitary operator

$$U(t) = \exp -iHt = \exp -iW\tau \quad (29)$$

$$\text{where, } W = 2xa^3H \Rightarrow \tau = \frac{t}{2xa^3} \quad (30)$$

For Trotterized time evolution, the total time $\tau = N_\tau\delta\tau$, where N_τ denotes the number of Trotter steps. If the value of the coupling changes, i.e. $x \rightarrow x'$, the scaled time

$$\tau \rightarrow \tau' = \frac{x}{x'}\tau \Rightarrow N'_\tau\delta\tau' = \frac{x}{x'}N_\tau\delta\tau. \quad (31)$$

If a Trotterized time evolution is performed without changing the size of the Trotter steps (i.e. $\delta\tau' = \delta\tau$), the number of Trotter steps required for evolving the system for a fixed duration of physical time is given by

$$N'_\tau = \frac{x}{x'}N_\tau. \quad (32)$$

We employ a first-order-Trotterized Schrödinger time evolution operator for unitaries constructed for

$$xH_I^{\text{approx}}, H_E^{\text{approx}} \ \& \ \mu H_M^{\text{approx}}$$

in that order, over a very short time $\delta\tau$ for each Trotter step. Evolving the system through N_τ steps span a total time of $\tau = N_\tau\delta\tau$. We choose $\delta\tau$ to be very short to minimize the Trotterization error and keep the same fixed to 0.0015 throughout the work.

Mapping string-ends to qubits

An open-boundary lattice of N sites is simulated on $2N$ qubits. The numbers $n_i(r)$ and $n_o(r)$ are directly mapped to individual qubits, whereas the $n_l(r)$ numbers can be recovered using (26). To make the qubits effectively fermions, the Jordan-Wigner transformation maps the ladder operators:

$$\begin{aligned} \hat{\chi}_i^-(r) &= \sigma^+(r) \prod_{r' < r} (-\sigma^z(r')) \\ \hat{\chi}_o^-(r) &= \sigma^+(r+L) \prod_{r' < r+L} (-\sigma^z(r')), \end{aligned} \quad (33)$$

where the qubit ladder operators are defined as

$$\begin{aligned} \sigma^+ &= \begin{pmatrix} 0 & 1 \\ 0 & 0 \end{pmatrix} \Rightarrow \sigma^+ |0\rangle = \sigma^+ \begin{pmatrix} 1 \\ 0 \end{pmatrix} = 0, \\ \sigma^+ |1\rangle &= \sigma^+ \begin{pmatrix} 0 \\ 1 \end{pmatrix} = \begin{pmatrix} 1 \\ 0 \end{pmatrix}. \end{aligned} \quad (34)$$

The Hermitian conjugates are $\hat{\chi}_i^+(r) = (\hat{\chi}_i^-(r))^\dagger$ and $\hat{\chi}_o^+(r) = (\hat{\chi}_o^-(r))^\dagger$, with $\sigma^- = (\sigma^+)^\dagger$.

The implied ordering of the variables where the first N represent the n_i quantum numbers, and the last N the n_o numbers, is relevant only within the mathematical construction, providing, for example, $\hat{\chi}^+\hat{\chi}^-$ products and the indices in matrix calculations. When considering the actual mapping to the hardware's qubits, a different ordering can be used. The qubit layout we choose is a zigzag (alternating) sequence of i and o quantum numbers:

$$|q_{2r}\rangle \equiv |n_i(r)\rangle, \quad |q_{2r+1}\rangle \equiv |n_o(r)\rangle. \quad (35)$$

This minimizes the number of SWAP layers throughout the circuit. Each $n_i(r)$ number needs to interact with both of its i neighbours, $n_i(r-1)$ and $n_i(r+1)$, and similarly for o numbers, while the electric Hamiltonian term acts on the $i-o$ pairs. All the SWAP gates required to enable this interaction can be arranged in two layers only for each trotter step (see Fig. 8), making this a highly efficient encoding whose depth depends only on the number of trotter steps, and not on the lattice site. Note that, in the initial Trotter step, the first layer of gates would have been the SWAPs to get the first interaction pairs adjacent, so the actual qubit initialization has an ordering that absorbs these SWAPs: $n_i(0), n_i(1), n_o(0), n_o(1), n_i(2), n_i(3), n_o(2), n_o(3), \dots$, while the layout at the end of each Trotter step follows the zigzag ordering above.

Building the Quantum Circuit

A single Trotter step applies the unitary

$$U(\delta\tau, c, \tilde{m}, \theta) = \underset{\text{small } \delta\tau}{\approx} e^{-i\delta\tau H'} e^{-i\tilde{m}H_M} e^{-i\delta\tau H_E} e^{-icH_I} \quad (36)$$

where $c = \delta\tau x$, $\tilde{m} = \delta\tau\mu$ are parameters appearing in the corresponding unitaries due to the interaction, and mass parts of the Hamiltonian.

The interaction part given in (28) translates into its qubit version as

$$H_I^{\text{approx}} = - \sum_{\substack{r=0 \\ r \neq N-1}}^{2N-2} [\sigma^-(r)\sigma^+(r+1) + \sigma^+(r)\sigma^-(r+1)] \quad (37)$$

The corresponding unitary takes the form

$$\begin{aligned} U_I &= e^{-i\delta\tau x H_I} \\ &\underset{\text{small } \delta\tau}{\approx} \prod_{r \neq N-1} \exp [ic (\sigma^-(r)\sigma^+(r+1) + \sigma^+(r)\sigma^-(r+1))] \\ &= \prod_{r \neq N-1} \exp \left[ic \begin{pmatrix} 0 & 0 & 0 & 0 \\ 0 & 0 & 1 & 0 \\ 0 & 1 & 0 & 0 \\ 0 & 0 & 0 & 0 \end{pmatrix}_{r \otimes r+1} \right] \\ &= \prod_{r \neq N-1} \begin{pmatrix} 1 & 0 & 0 & 0 \\ 0 & \cos c & i \sin c & 0 \\ 0 & i \sin c & \cos c & 0 \\ 0 & 0 & 0 & 1 \end{pmatrix}_{r \otimes (r+1)} \end{aligned} \quad (38)$$

Here $c = \delta_\tau x$ is a real constant. Since each non-boundary-site qubit appears in two of the factors, corresponding to hopping in two directions, the algorithm is split into two layers with SWAP gates in between. Using matrix multiplication, the two-qubit hopping term in (37) is uncovered in terms of standard single- and two-qubit gates:

$$U_{I,r\otimes(r+1)} = CNOT_{(r+1)\otimes r}(1 \otimes H) CNOT_{r\otimes(r+1)} \\ (1 \otimes R_z(c)) CNOT_{r\otimes(r+1)} (1 \otimes R_z(-c)) \\ (1 \otimes H) CNOT_{(r+1)\otimes r} \quad (39)$$

After the two layers of this hopping unitary, SWAP gates get the qubits into the zigzag position for the electric and mass terms to be applied.

The electric part is

$$H_E = N h_E^0 + \sum_{\{r'\}} \left(\frac{n_l}{2} + \frac{3}{4} \right) \quad (40)$$

with $\{r'\}$ denoting the set of sites in the fermion configuration 01 (corresponding to the second entry in the 2-qubit tensor product). The first term gives a global phase to the evolution of qubits, so we ignore it. This is also an approximation because the value of the average flux h_E^0 differs between basis states, but we approximate it to always be equal to the boundary flux. However, the phase correction in the 01 case at every site and its entangling properties can be seen to increase the validity of the simulation. This second term in H_E is translated into a circuit applied on each site's qubit pair, which gives a certain phase in the required 01 case, and a different phase in the other three cases (same for all three):

$$U_{E,x\otimes(r+1)}(\theta) = (r \otimes R_z(\theta/2)) CNOT_{x\otimes(r+1)} (1 \otimes R_z(-\theta/2)) \\ CNOT_{x\otimes(r+1)} (R_z(\theta/2) \otimes 1) (r \otimes 1) \\ = \begin{pmatrix} e^{-i\theta/4} & 0 & 0 & 0 \\ 0 & e^{i3\theta/4} & 0 & 0 \\ 0 & 0 & e^{-i\theta/4} & 0 \\ 0 & 0 & 0 & e^{-i\theta/4} \end{pmatrix}_{x\otimes(r+1)} \quad (41)$$

which is a global phase plus an $e^{i\theta}$ phase in the desired case. The x and $x+1$ here correspond to the n_i, n_o pair of any single lattice site.

θ can be identified from the desired phase

$$e^{-i\delta_\tau \left(\frac{n_l}{2} + \frac{3}{4} \right)} = e^{i\theta} \implies \theta = -\delta_\tau \left(\frac{n_l}{2} + \frac{3}{4} \right) \quad (42)$$

The mass term H_M adds a phase to each qubit:

$$\mu H_M = \mu \sum_r (-1)^r (n_i(r) + n_o(r)) \quad (43)$$

$$e^{-i\delta_\tau \mu H_M} = \prod_r e^{i(-1)^{r+1} \tilde{m} n_i(r)} e^{i(-1)^{r+1} \tilde{m} n_o(r)} \\ = \prod_{r \text{ even}} R_z(-\tilde{m})_{2r} R_z(-\tilde{m})_{2r+1} \\ \prod_{r \text{ odd}} R_z(\tilde{m})_{2r} R_z(\tilde{m})_{2r+1} \quad (44)$$

where $\tilde{m} = \delta_\tau \mu$. The R_z gates are applied at the end of each Trotter step.

Proof of Concept

The algorithm is simulated classically for small numbers of qubits. For a 6-site lattice (12 qubits), ideal simulation of the quantum circuit is compared to exact diagonalization results by plotting the total particle number over time for both cases. Exact diagonalization takes the full LSH Hamiltonian as given in (14), (15) and (16). The calculation of dynamics is also exact via simple matrix multiplication, and free from any Trotterization approximation. Comparison of the dynamics for the original theory and the same obtained via ideal simulation of the quantum circuit is presented in Fig. 7.

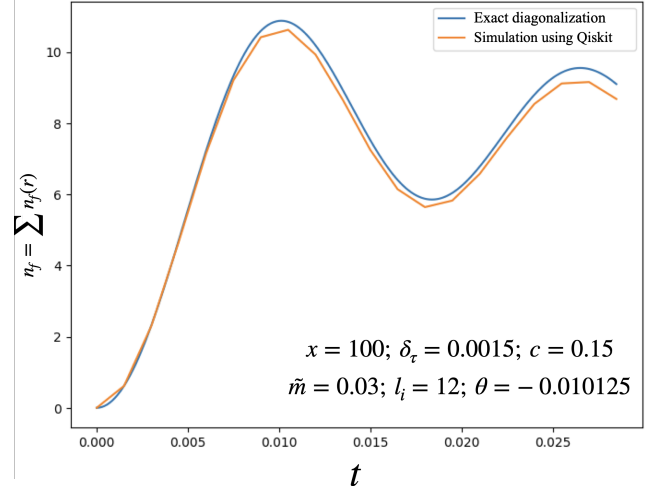


Fig. 7: Proof of concept. Particle number for a lattice of 6 sites as calculated from qubit expectation values at each Trotter step using Qiskit simulator, compared with the exact diagonalization result for the full LSH Hamiltonian, which is free from any Trotterization error and approximation error. Parameters in the quantum circuit are chosen to reproduce the intended regime of the theory with $x = 100$ and $m/g = 1$. The initial state is chosen to be the strong coupling vacuum, which is a computational basis state.

Scaling up the quantum simulation

With the benchmarking of the parameters as presented in Fig. 7, we proceed towards large scale implementations of the quantum circuit (Fig. 8) using *IBM BOSTON* (156 qubit HERON processor).

Experimental measurement from QPU

We implement trotterized time evolution with a circuit depth that is independent of system size. Each Trotter step comprises two SWAP layers to mediate nearest-neighbor interactions; for steps $t_{\text{trot}} \geq 2$ we prepend a single additional SWAP layer to account for the initial zigzag configuration of qubits. Because the circuit layout is isomorphic to the device topology, qubit mapping requires no extra SWAPs. The Qiskit transpiler is used solely to (i) select a low-noise linear chain of physical qubits and (ii) decompose the circuit to the native gate set of the device.

At each Trotter step, we estimate $\langle \sigma_z \rangle$ for every qubit and infer the excited-state occupancy via $P(1) = \frac{1 - \langle \sigma_z \rangle}{2}$. Expectation-value estimation enables error-mitigation workflows, and keeps the path open for future application of state-of-the-art

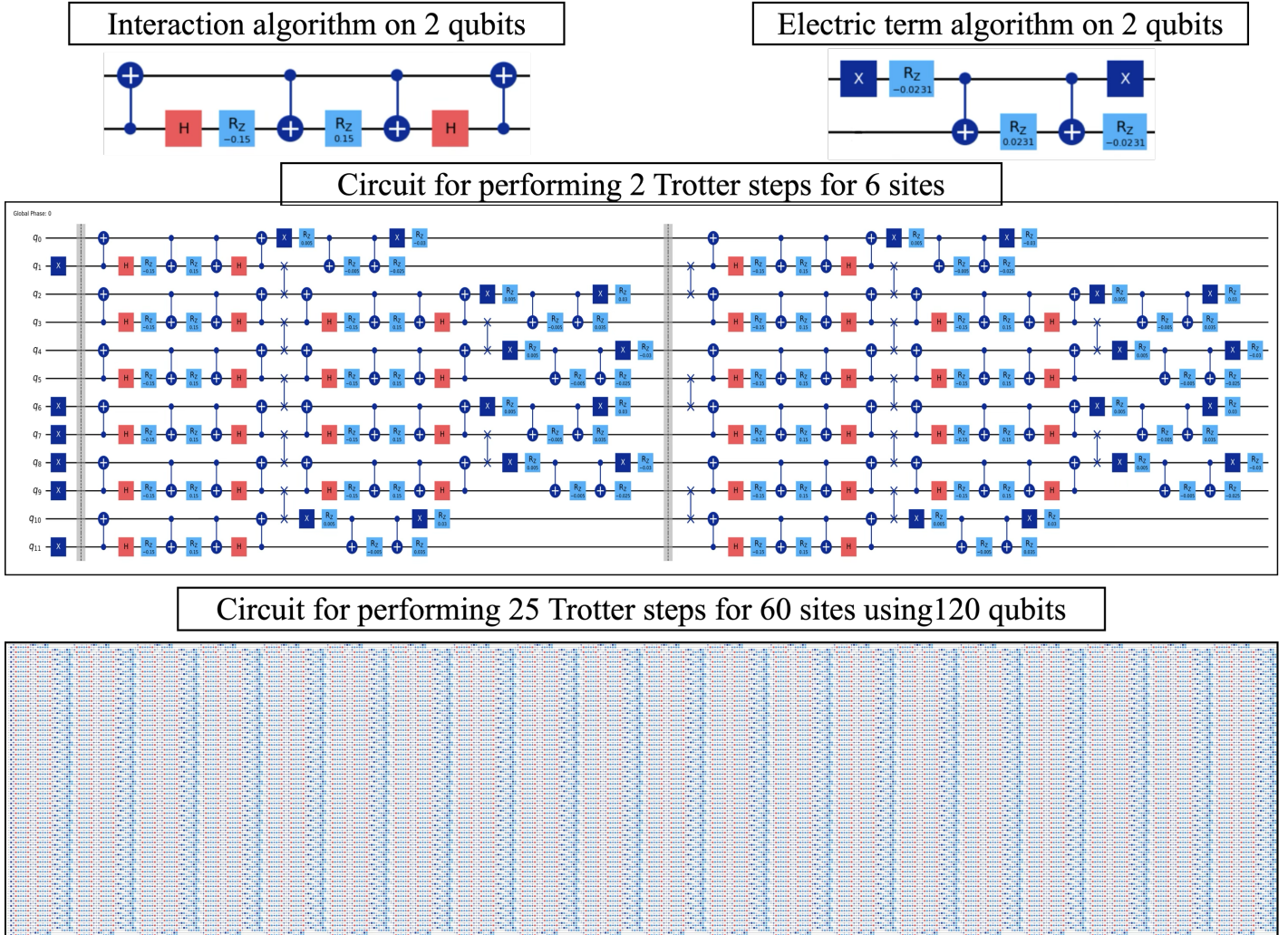


Fig. 8: The Quantum Circuit: implements unitaries constructed for each term of the Hamiltonian. The mass Hamiltonian is a single qubit rotation, while the building block of electric term and interaction term of the Hamiltonian are 2-qubit operations. Use of a number of swap gates allows simultaneous application of the unitaries for both in a single Trotter step. The middle panel presents two Trotter steps of the full algorithm over 6 lattice sites, initialized with a pair of hadron-antihadron at the center. The bottom panel presents the quantum circuit employed in this study upto 25 Trotter steps of the full algorithm over 60 lattice sites for $x = 100$, initialized with a meson at the center. The full circuit consists of 17660 2-qubit gates and over 90000 single-qubit gates.

error mitigation; in this work we apply measurement-error mitigation to correct readout bias. Following these strategies, we simulate a 60-site staggered SU(2) lattice using 120 qubits (two qubits per site). The two-qubit depth for t Trotter steps is $13t - 1$, where the -1 accounts for a bypassed SWAP layer enabled by the zigzag qubit initialization. Thus, at $t = 25$, the circuit has two-qubit depth 324 and comprises 17,660 two-qubit gates with a total gate count of 90,955, the largest reported till date.

No exact classical method is available at this scale. For validation, we compare the hardware results against approximate tensor-network simulations and approximate Pauli-propagation method.

Benchmarking via TN

In this section, we briefly outline the Matrix Product State (MPS) ansatz used to benchmark the QPU results. Classical Tensor Network (TN) methods have emerged as powerful tools to study properties of low-dimensional quantum systems [55, 56]. Of late, they have been used to explore static and dynamic properties of lattice gauge theories, see Ref.[57] for a comprehensive review on this topic. In this context, we have developed a tensor network ansatz for the Loop-String-Hadron formulation [43], whereby one can calculate static and dynamic properties of this theory. We will skip the details of the implementations and briefly explain the essentials to establish the workflow. The ansatz is defined for the full LSH Hamiltonian given in Eq. 13. Accordingly, all subsequent definitions of the Hilbert space and the associated operators are formulated with respect to the full theory. The full Hilbert space at each site is characterized by a set of three quantum numbers $|n_l, n_i, n_o\rangle$ and the MPS ansatz is directly endowed with this structure. Formally, one can write it down as follows:

$$|\Psi[A]\rangle = \sum_{p_1, \dots, p_N} A_{p_1}^{\alpha_1} A_{p_2}^{\alpha_1, \alpha_2} \dots A_{p_N}^{\alpha_{N-1}} |p_1, p_2, \dots, p_N\rangle. \quad (45)$$

Here, p_r corresponds to the physical states at each lattice site r . The notation $|p_1, p_2, \dots, p_N\rangle \equiv \otimes_{r=1}^N |p_r\rangle$, where $|p_r\rangle \equiv |n_l, n_i, n_o\rangle_r$. The variational degrees of freedom are contained in the A -matrices, which is defined at each sites and populated by complex entries. We further impose the two global symmetries of the LSH Hamiltonian, namely \mathcal{B} and q into the local tensor structure to yield a blocksparse representation. We rely on the ITensors.jl library [58, 59] and its inbuilt functions to construct the MPS/MPO functions. For time-evolving the initial state, we use the 2-site time-dependent variational principle (TDVP) algorithm [60] defined in the library. Due to computational overhead with the 2-site algorithm, we have opted to keep the maximum bond-dimension to 200. This will result in errors accumulating as the time evolution progresses, and is reflected in the entanglement entropy plot in Fig. 6. Tabulated values this error is presented in the Supplementary information. The simulation is set up for each value of $x \in \{50, 100, 200\}$ by first initializing two product state MPSes, one for the strong-coupling vacuum state and the other for the string-configurations. Both of these states correspond to the same symmetry sector of the LSH Hamiltonian and the algorithm trivially conserves these quantum numbers by construction. The relevant observables are computed for both these time evolved states and subtract to isolate the evolution of the initialized meson.

Benchmarking via PP

We benchmark quantum processing unit (QPU) observables using the Pauli Propagation Method (PP) [28], a

Heisenberg-picture simulator that back-propagates the measured observable O through the circuit partitioned into logical layers. Under Clifford evolution, Pauli operators map to Pauli operators; consequently, purely Clifford layers preserve the operator's Pauli support and do not increase the number of qubit-wise non-commuting terms. By contrast, a non-Clifford layer whose generator anticommutes with a Pauli component of O can induce branching: in the worst case, the number of Pauli terms doubles across such a layer, leading to exponential growth in the term count with circuit depth. To bound the computational cost, one may truncate by discarding Pauli terms whose coefficients fall below a prescribed threshold during back-propagation, trading accuracy for tractability in a controlled manner.

In this work, we target non-truncated PP, i.e., back-propagation proceeds without discarding terms, rendering the result effectively exact up to floating-point tolerances. Since there is no immediate way to identify the number of Pauli terms required to backpropagate the circuit completely and exactly, to set a safe compute budget, we empirically upper-bounded the Pauli-term cardinality at the circuit input as follows: we tracked (i) the number of Pauli terms and (ii) the remaining layer depth over an initial segment of the back-propagation, then extrapolated to depth zero. The inferred terminal term counts were 9,400, 12,500, and 66,000 for $x = 50, 100$ and 200 , respectively. Within these budgets, back-propagation is *expected* to be completed without, or minor, truncation. Accordingly, the PP estimates serve as reference values for the corresponding QPU observables at these settings and scales.

We also implement the PP algorithm on GPUs using NVIDIA's cuQuantum library, specifically the cuPauliProp API together with CUDA for memory management and parallel execution [61, 62]. In PP method, the observables are represented as Pauli expansions $O = \sum_k c_k P_k$, where P_k are packed Pauli strings and c_k are real coefficients. Starting from an initial local observable such as Z_q acting on qubit q , the PP algorithm repeatedly conjugates the operator with the circuit gates, which generates a growing linear combination of Pauli strings represented on the GPU using cupaulipropPauliExpansion data structures. Since the number of Pauli terms increases rapidly with circuit depth, we employ a coefficient-based truncation strategy. After each operator application, Pauli terms whose coefficients satisfy $|c_k| < \epsilon$ are discarded, where we choose the cutoff $\epsilon = 10^{-5}$. To maintain a compact representation of the Pauli expansion, the GPU performs a parallel radix sort to group identical Pauli strings, followed by a parallel reduction that merges duplicates and sums their coefficients. During this compaction step, terms with coefficients below the cutoff are removed. This procedure trades a controlled amount of numerical precision for substantial reductions in memory usage and runtime. The truncation is implemented using the CUPAULIPROP_TRUNCATION_STRATEGY_COEFFICIENT_BASED option provided by the cuPauliProp library. All Pauli expansions, coefficient arrays, and intermediate buffers remain resident in GPU memory to avoid host-device data transfers, while dedicated scratch workspace buffers are allocated for the operator-application kernels. After the observable has been propagated through the circuit, its expectation value is evaluated in the computational zero state, (representing the strong coupling vacuum) $\langle O \rangle = \langle 0^{\otimes n} | O(t) | 0^{\otimes n} \rangle$, where only Pauli strings composed entirely of Z and identity operators contribute to the trace. This trace is computed on the GPU using the cupaulipropPauliExpansionViewComputeTraceWithZeroState routine. The complete simulation workflow therefore consists

of generating a Trotterized quantum circuit, initializing the observable $O = Z_q$ for each qubit q , constructing a single-term Pauli expansion, propagating the operator through the circuit in reverse order with truncation applied after each gate, computing the expectation value $\langle Z_q(t) \rangle$, and repeating the procedure for all qubits and Trotter steps. This GPU-based implementation enables efficient evaluation of local observables in large quantum circuits while controlling the exponential growth of the Pauli expansion through coefficient truncation.

Estimating Errors

In this work, we report error bar for the dynamical observable particle density $n_f(t)$ defined as the sum of particle-antiparticle number at each lattice sites $n_f(r, t)$. With the quantum experiment using a QPU, and the three approximate classical benchmarks, we obtain four independent estimates for the observable, (without any prior knowledge of the true value)

$$n_f^{(m)}(t), m \in \{\text{TN}, \text{PP} - \text{CPU}, \text{PP} - \text{GPU}, \text{QPU}\}.$$

The median of these distributions is chosen as the reference, along with the standard deviation of these 4 data sets at each time slices,

$$\begin{aligned} \sigma_{\text{std}}(t) &= \sqrt{\frac{1}{3} \sum_m \left(n_f^{(m)}(t) - \bar{n}_f(t) \right)^2}, \quad (46) \\ \text{with } \bar{n}_f(t) &= \frac{1}{4} \sum_m n_f^{(m)}(t), \quad (47) \end{aligned}$$

denoting an intrinsic method-to-method uncertainty. We further note that, the observable $n_f(r, t)$ is directly related to measuring $n_i + n_o$ excitations at each site while the same quantity contributes to a conserved global charge $\mathcal{B} + N = Q = \sum_r n_i(r) + n_o(r) = 60$. We monitor global-symmetry conservation through the total charge

$$\Delta Q^{(m)}(t) = Q^{(m)}(t) - 60, \quad (48)$$

and convert this constraint violation into an additional error scale. Assuming Q is a sum over $L = 60$ sites, we use the conservative per-site scaling $\Delta Q^{(m)}(t)/\sqrt{L}$ and define a method-aggregated constraint term by the RMS

$$\Delta Q_{\text{rms}}(t) = \sqrt{\frac{1}{4} \sum_m \left(\Delta Q^{(m)}(t) \right)^2}. \quad (49)$$

Our final reported reference value with shared uncertainty band ($n_f^{\text{ref}}(t) \pm \sigma_{\text{shared}}(t)$) around the reference curve is obtained by quadrature,

$$\sigma_{\text{shared}}(t) = \sqrt{\sigma_{\text{std}}(t)^2 + \left(\frac{\Delta Q_{\text{rms}}(t)}{\sqrt{60}} \right)^2}, \quad (50)$$

which captures both cross-method variability and global-constraint inconsistency.

Additionally, for each method we report individual error bars

$$\sigma_m(t) = \sqrt{\sigma_{\text{m.pair}}(t)^2 + \left(\frac{|\Delta Q^{(m)}(t)|}{\sqrt{60}} \right)^2},$$

where

$$\sigma_{\text{m.pair}}(t) = |n_f^{(m)}(t) - n_f^{\text{ref}}(t)|.$$

The deviations from global conservation inflate the uncertainty in a controlled and transparent manner.

End Notes

The foundation of the current experiment lie on LSH encoding, followed by the weak coupling approximation detailed in the Methods. This approximation is essential to come up with an implementable quantum algorithm for the complicated dynamics using restricted number of qubits with restricted connectivity on the *IBM Heron* processors. A very important conclusion from the outcome of classical benchmarking is establishing the validity of the approximation for the coupling regime of interest. The value of observables obtained via the PP (classical GPU simulation of the approximated LSH Hamiltonian) and the same obtained via TN (classical simulation of the full LSH Hamiltonian) agree up to an average standard deviation of 0.01 over all time slices.

The average value of the error bar (defined for cross-method validation) associated with the observable n_f for QPU is obtained as 0.0973, while the same for PP-CPU is 0.0406. The TN and PP-GPU have relatively smaller error bars, with average magnitudes of 0.0184 and 0.0128, respectively. However, given that all four error bars are of the same order for the reported observable, the quantum data without active error mitigation may still be useful for extracting physical information.

A technical remark on imposing the bosonic cut-off in this computation is worth mentioning here. In the LSH framework, the cut-off corresponds to the maximum amount of gauge flux allowed on each link. The approximation scheme is set up for an arbitrarily large value of the cut-off as we consider a large amount of flux to enter and exit the lattice. The same is equally valid for the quantum algorithm and its implementation using a QPU and a PP. However, the TN algorithm can only work with a finite cut-off; we choose the value of the cut-off to be SIX for the TN benchmark. The value of the phase angle θ in the quantum algorithm is chosen to match this limitation on the cut-off. In principle, this particular quantum algorithm allows computations to be performed with a larger cut-off, and goes beyond the scope of TN calculations.

In Fig. 6, we provide a quantitative comparison of the benchmarks for three different values of x . It is found that as the system approaches the weak-coupling or continuum limit, the quantum processor maintains structural robustness where classical tensor networks and Pauli propagation methods encounter deviation from physicality within the capacity of available classical computing resources. Quantum processor maintains structural robustness as reflected in the consistent oscillatory behaviour of the number density with respect to time. Violation of global symmetries, albeit minimal for PP and QPU both, grows systematically with increasing x for longer time for PP, while remains of the same order for QPU at all values of x and at all time scales. A careful look into the high fidelity results from QPU suggests a lightcone to emerge as an outcome of the differential measurement for all values of x similar to the same obtained via PP. This is indeed nontrivial given the scale of the circuit it implements (see Fig. 8).

These observations suggest the possibility of a robust quantum simulation strategy for notoriously difficult non-Abelian gauge theories and point towards a road map for useful quantum advantage once hardware noise subsides.

References

- [1] Martinez, E. A. *et al.* Real-time dynamics of lattice gauge theories with a few-qubit quantum computer. *Nature* **534**, 516–519 (2016). [1605.04570](#).
- [2] Yang, B. *et al.* Observation of gauge invariance in a 71-site Bose–Hubbard quantum simulator. *Nature* **587**, 392–396 (2020). [2003.08945](#).
- [3] Mil, A. *et al.* A scalable realization of local U(1) gauge invariance in cold atomic mixtures. *Science* **367**, 1128–1130 (2020). [1909.07641](#).
- [4] Mildenerger, J., Mruczkiewicz, W., Halimeh, J. C., Jiang, Z. & Hauke, P. Confinement in a \mathbb{Z}_2 lattice gauge theory on a quantum computer. *Nature Phys.* **21**, 312–317 (2025). [2203.08905](#).
- [5] Meth, M. *et al.* Simulating two-dimensional lattice gauge theories on a qudit quantum computer. *Nature Phys.* **21**, 570–576 (2025). [2310.12110](#).
- [6] Cochran, T. A. *et al.* Visualizing dynamics of charges and strings in (2 + 1)D lattice gauge theories. *Nature* **642**, 315–320 (2025). [2409.17142](#).
- [7] Zhou, Z.-Y. *et al.* Thermalization dynamics of a gauge theory on a quantum simulator. *Science* **377**, abt6277 (2022). [2107.13563](#).
- [8] Mueller, N., Wang, T., Katz, O., Davoudi, Z. & Cetina, M. Quantum computing universal thermalization dynamics in a (2 + 1)D Lattice Gauge Theory. *Nature Commun.* **16**, 5492 (2025). [2408.00069](#).
- [9] Schweizer, C. *et al.* Floquet approach to \mathbb{Z}_2 lattice gauge theories with ultracold atoms in optical lattices. *Nature Phys.* **15**, 1168–1173 (2019). [1901.07103](#).
- [10] Mueller, N. *et al.* Quantum Computation of Dynamical Quantum Phase Transitions and Entanglement Tomography in a Lattice Gauge Theory. *PRX Quantum* **4**, 030323 (2023). [2210.03089](#).
- [11] Farrell, R. C., Illa, M., Ciavarella, A. N. & Savage, M. J. Quantum simulations of hadron dynamics in the Schwinger model using 112 qubits. *Phys. Rev. D* **109**, 114510 (2024). [2401.08044](#).
- [12] Davoudi, Z., Hsieh, C.-C. & Kadam, S. V. Scattering wave packets of hadrons in gauge theories: Preparation on a quantum computer. *Quantum* **8**, 1520 (2024). [2402.00840](#).
- [13] Cobos, J. *et al.* Real-Time Dynamics in a (2+1)-D Gauge Theory: The Stringy Nature on a Superconducting Quantum Simulator. *arXiv preprint arXiv:2507.08088* (2025). [2507.08088](#).
- [14] Gonzalez-Cuadra, D. *et al.* Observation of string breaking on a (2 + 1)D Rydberg quantum simulator. *Nature* **642**, 321–326 (2025). [2410.16558](#).
- [15] Xiang, D.-S. *et al.* Real-time scattering and freeze-out dynamics in Rydberg-atom lattice gauge theory (2025). [2508.06639](#).
- [16] Klco, N., Stryker, J. R. & Savage, M. J. SU(2) non-Abelian gauge field theory in one dimension on digital quantum computers. *Phys. Rev. D* **101**, 074512 (2020). [1908.06935](#).
- [17] Ciavarella, A., Klco, N. & Savage, M. J. Trailhead for quantum simulation of SU(3) Yang-Mills lattice gauge theory in the local multiplet basis. *Phys. Rev. D* **103**, 094501 (2021). [2101.10227](#).
- [18] Atas, Y. Y. *et al.* SU(2) hadrons on a quantum computer via a variational approach. *Nature Commun.* **12**, 6499 (2021). [2102.08920](#).
- [19] Atas, Y. Y. *et al.* Simulating one-dimensional quantum chromodynamics on a quantum computer: Real-time evolutions of tetra- and pentaquarks. *Phys. Rev. Res.* **5**, 033184 (2023). [2207.03473](#).
- [20] Ciavarella, A. N. & Bauer, C. W. Quantum Simulation of SU(3) Lattice Yang-Mills Theory at Leading Order in Large-Nc Expansion. *Phys. Rev. Lett.* **133**, 111901 (2024). [2402.10265](#).
- [21] Farrell, R. C. *et al.* Preparations for quantum simulations of quantum chromodynamics in 1+1 dimensions. I. Axial gauge. *Phys. Rev. D* **107**, 054512 (2023). [2207.01731](#).
- [22] Farrell, R. C. *et al.* Preparations for quantum simulations of quantum chromodynamics in 1+1 dimensions. II. Single-baryon β -decay in real time. *Phys. Rev. D* **107**, 054513 (2023). [2209.10781](#).
- [23] Chernyshev, I. A. *et al.* Pathfinding quantum simulations of neutrinoless double- β decay. *Nature Commun.* **17**, 1826 (2026). [2506.05757](#).
- [24] Bauer, C. W., Davoudi, Z., Klco, N. & Savage, M. J. Quantum simulation of fundamental particles and forces. *Nature Rev. Phys.* **5**, 420–432 (2023). [2404.06298](#).
- [25] Di Meglio, A. *et al.* Quantum Computing for High-Energy Physics: State of the Art and Challenges. *PRX Quantum* **5**, 037001 (2024). [2307.03236](#).
- [26] Raychowdhury, I. & Stryker, J. R. Loop, string, and hadron dynamics in SU(2) Hamiltonian lattice gauge theories. *Phys. Rev. D* **101**, 114502 (2020). [1912.06133](#).
- [27] Berg, E. v. d., Mineev, Z. K. & Temme, K. Model-free readout-error mitigation for quantum expectation values. *Phys. Rev. A* **105**, 032620 (2022). [2012.09738](#).
- [28] Rudolph, M. S., Jones, T., Teng, Y., Angrisani, A. & Holmes, Z. Pauli Propagation: A Computational Framework for Simulating Quantum Systems. *arXiv preprint arXiv:2505.21606* (2025). [2505.21606](#).
- [29] Amorosso, R., Syritsyn, S. & Venugopalan, R. Entanglement entropy of a color flux tube in (2+1)D Yang-Mills theory. *JHEP* **12**, 177 (2024). [2410.00112](#).
- [30] Altmann, J., Dubla, A., Greco, V., Rossi, A. & Skands, P. Towards the understanding of heavy quarks hadronization: from leptonic to heavy-ion collisions. *Eur. Phys. J. C* **85**, 16 (2025). [2405.19137](#).
- [31] Müller, B. & Schäfer, A. Quark-Hadron Transition and Entanglement (2022). [2211.16265](#).
- [32] Kogut, J. B. & Susskind, L. Hamiltonian Formulation of Wilson’s Lattice Gauge Theories. *Phys. Rev. D* **11**, 395–408 (1975).
- [33] Hamer, C. J., Oitmaa, J. & Zheng, W.-H. Series analysis of U(1) and SU(2) lattice gauge theory in (2+1)-dimensions. *Phys. Rev. D* **45**, 4652–4658 (1992).
- [34] Kim, Y. *et al.* Evidence for the utility of quantum computing before fault tolerance. *Nature* **618**, 500–505 (2023).
- [35] Mathur, M. Harmonic oscillator prepotentials in SU(2) lattice gauge theory. *J. Phys. A* **38**, 10015–10026 (2005). [hep-lat/0403029](#).
- [36] Mathur, M. Loop Approach to Lattice Gauge Theories. *Nucl. Phys. B* **779**, 32–62 (2007). [hep-lat/0702007](#).

- [37] Anishetty, R. & Raychowdhury, I. SU(2) lattice gauge theory: Local dynamics on nonintersecting electric flux loops. *Phys. Rev. D* **90**, 114503 (2014). [1408.6331](#).
- [38] Raychowdhury, I. Low energy spectrum of SU(2) lattice gauge theory: An alternate proposal via loop formulation. *Eur. Phys. J. C* **79**, 235 (2019). [1804.01304](#).
- [39] Davoudi, Z., Shaw, A. F. & Stryker, J. R. General quantum algorithms for Hamiltonian simulation with applications to a non-Abelian lattice gauge theory. *Quantum* **7**, 1213 (2023). [2212.14030](#).
- [40] Dasgupta, R. & Raychowdhury, I. Cold-atom quantum simulator for string and hadron dynamics in non-Abelian lattice gauge theory. *Phys. Rev. A* **105**, 023322 (2022). [2009.13969](#).
- [41] Muller, B. & Schafer, A. Entropy Creation in Relativistic Heavy Ion Collisions. *Int. J. Mod. Phys. E* **20**, 2235–2267 (2011). [1110.2378](#).
- [42] Ebner, L. *et al.* Entanglement properties of SU(2) gauge theory. *Commun. Phys.* **8**, 368 (2025). [2411.04550](#).
- [43] Mathew, E. *et al.* Tensor-network toolbox for probing dynamics of non-Abelian gauge theories. *PoS LATTICE2024*, 472 (2025). [2501.18301](#).
- [44] Das, D. *et al.* Eigenstate Thermalization in 1+1-Dimensional SU(2) Lattice Gauge Theory Coupled with Dynamical Fermions (2025). [2509.18269](#).
- [45] Raychowdhury, I. *Prepotential Formulation of Lattice Gauge Theories*. Ph.D. thesis, Calcutta U. (2013).
- [46] Kadam, S. V., Raychowdhury, I. & Stryker, J. R. Loop-string-hadron formulation of an su(3) gauge theory with dynamical quarks. *Phys. Rev. D* **107**, 094513 (2023). URL <https://link.aps.org/doi/10.1103/PhysRevD.107.094513>.
- [47] Kadam, S. V., Naskar, A., Raychowdhury, I. & Stryker, J. R. Loop-string-hadron approach to su(3) lattice yang-mills theory: Hilbert space of a trivalent vertex. *Phys. Rev. D* **111**, 074516 (2025). URL <https://link.aps.org/doi/10.1103/PhysRevD.111.074516>.
- [48] Kadam, S. V., Naskar, A., Raychowdhury, I. & Stryker, J. R. Loop-string-hadron approach to su(3) lattice yang-mills theory, ii: Operator representation for the trivalent vertex (2025). URL <https://arxiv.org/abs/2512.11796>. [2512.11796](#).
- [49] Lanes, O. *et al.* A framework for quantum advantage (2025). URL <https://arxiv.org/abs/2506.20658>. [2506.20658](#).
- [50] Mathur, M., Raychowdhury, I. & Anishetty, R. SU(N) Irreducible Schwinger Bosons. *J. Math. Phys.* **51**, 093504 (2010). [1003.5487](#).
- [51] Anishetty, R., Mathur, M. & Raychowdhury, I. Irreducible SU(3) Schwinger Bosons. *J. Math. Phys.* **50**, 053503 (2009). [0901.0644](#).
- [52] Anishetty, R., Mathur, M. & Raychowdhury, I. Prepotential formulation of SU(3) lattice gauge theory. *J. Phys. A* **43**, 035403 (2010). [0909.2394](#).
- [53] Raychowdhury, I. & Anishetty, R. Prepotential Formulation of Lattice Gauge Theory. *PoS LATTICE2014*, 313 (2014). [1411.3068](#).
- [54] Davoudi, Z., Raychowdhury, I. & Shaw, A. Search for efficient formulations for Hamiltonian simulation of non-Abelian lattice gauge theories. *Phys. Rev. D* **104**, 074505 (2021). [2009.11802](#).
- [55] Schollwoeck, U. The density-matrix renormalization group in the age of matrix product states. *Annals Phys.* **326**, 96–192 (2011). [1008.3477](#).
- [56] Bañuls, M. C. Tensor Network Algorithms: A Route Map. *Ann. Rev. Condensed Matter Phys.* **14**, 173–191 (2023). [2205.10345](#).
- [57] Bañuls, M. C. & Cichy, K. Review on Novel Methods for Lattice Gauge Theories. *Rept. Prog. Phys.* **83**, 024401 (2020). [1910.00257](#).
- [58] Fishman, M., White, S. R. & Stoudenmire, E. M. The ITensor Software Library for Tensor Network Calculations. *SciPost Phys. Codebases* **4** (2022). URL <https://scipost.org/10.21468/SciPostPhysCodeb.4>.
- [59] Fishman, M., White, S. R. & Stoudenmire, E. M. Codebase release 0.3 for ITensor. *SciPost Phys. Codebases* **4-r0.3** (2022). URL <https://scipost.org/10.21468/SciPostPhysCodeb.4-r0.3>.
- [60] Paeckel, S. *et al.* Time-evolution methods for matrix-product states. *Annals Phys.* **411**, 167998 (2019). [1901.05824](#).
- [61] Bayraktar, H. *et al.* cuquantum sdk: A high-performance library for accelerating quantum science. In *2023 IEEE International Conference on Quantum Computing and Engineering (QCE)*, vol. 01, 1050–1061 (2023).
- [62] NVIDIA Corporation. cupauliprop: A high-performance library for pauli propagation quantum simulators. <https://docs.nvidia.com/cuda/cuquantum/latest/cupauliprop/overview.html> (2026). NVIDIA cuQuantum documentation, accessed 2026-03-11.

Supplementary Information

The values of the individual error bars reported in Fig. 5 are listed in the Table 3.

Quantum simulation vs. classical simulation

The details of the runtime for each Trotter step using each method for $x = 100$ are tabulated in Table 1.

Table 1: Data Comparison: Execution Times

Trotter step	QPU (sec)	TN (sec)	PP-CPU (sec)	PP-GPU (sec)
1	20	170.106	23.2512	90.2822
2	20	200.972	114.6801	199.2602
3	20	290.948	232.8814	312.8630
4	20	423.376	352.9601	428.8070
5	20	584.092	477.4471	547.5810
6	20	786.466	592.9340	668.0500
7	20	1180.006	726.0387	792.5720
8	20	1994.450	850.0756	919.3930
9	20	3223.432	981.8030	1051.3070
10	20	4936.112	1111.2079	1186.1290
11	20	7616.980	1246.4771	1327.1470
12	20	9408.224	1355.9682	1476.8920
13	20	9408.224	1517.3462	1638.0440
14	20	9457.832	1606.2973	1809.1480
15	20	11300.992	1798.2811	1990.1430
16	20	10530.030	1912.3661	2173.8900
17	20	8936.264	2054.6526	2357.6000
18	20	8905.564	2233.0782	2543.8400
19	20	9148.052	2351.2184	2734.2200
20	20	8949.110	2484.3693	2930.4400

The estimated error in the tensor network calculation is directly related to the errors building up as the time evolution progresses due to finite bond dimension. This error corresponds to the sum of the Schmidt values that were discarded after each time step as tabulated in Table 2.

Trotter step	Truncation Error		
	$x = 200$	$x = 100$	$x = 50$
1	10^{-11}	10^{-11}	10^{-11}
2	10^{-11}	10^{-11}	10^{-11}
3	10^{-11}	10^{-11}	10^{-11}
4	10^{-11}	10^{-11}	10^{-11}
5	10^{-11}	10^{-11}	10^{-11}
6	10^{-9}	10^{-11}	10^{-11}
7	10^{-7}	10^{-11}	10^{-11}
8	10^{-6}	10^{-11}	10^{-11}
9	10^{-4}	10^{-11}	10^{-11}
10	10^{-3}	10^{-11}	10^{-11}
11	10^{-3}	10^{-10}	10^{-11}
12	10^{-3}	10^{-9}	10^{-11}
13	10^{-2}	10^{-8}	10^{-11}
14	10^{-2}	10^{-7}	10^{-11}
15	10^{-2}	10^{-6}	10^{-11}
16	10^{-3}	10^{-5}	10^{-11}
17	10^{-3}	10^{-5}	10^{-11}
18	10^{-3}	10^{-4}	10^{-11}
19	10^{-3}	10^{-4}	10^{-11}
20	10^{-3}	10^{-4}	10^{-11}

Table 2: The maximum truncation error in the Schmidt values for the time evolved state at each TDVP time step

Trotter step	Magnitude of error bars for			
	TN	PP-CPU	PP-GPU	QPU
1	0.000393	0.000393	0.000394	0.037981
2	0.001433	0.002093	0.001433	0.078603
3	0.007679	0.001600	0.001600	0.004534
4	0.014291	0.004468	0.004468	0.052748
5	0.022174	0.009427	0.009427	0.077490
6	0.030052	0.016143	0.016143	0.157964
7	0.036875	0.023230	0.023230	0.170741
8	0.041701	0.029011	0.028255	0.028320
9	0.007022	0.068981	0.007037	0.016977
10	0.007009	0.068038	0.007017	0.170568
11	0.005745	0.063114	0.005752	0.191280
12	0.003736	0.056778	0.003827	0.174985
13	0.002753	0.051557	0.003012	0.161465
14	0.003788	0.049230	0.003976	0.013341
15	0.034967	0.023118	0.023093	0.049691
16	0.042817	0.029218	0.029168	0.130727
17	0.049697	0.038766	0.038798	0.090731
18	0.042992	0.061825	0.037303	0.038343
19	0.000899	0.111911	0.002302	0.081743
20	0.011387	0.103556	0.011421	0.239686

Table 3: List of the values of the error bars for each method per time slice for computation at $x = 100$.

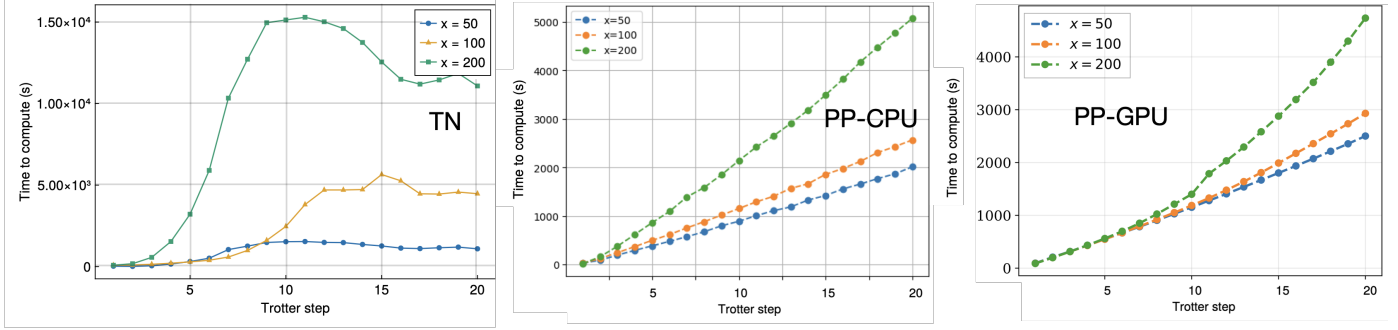


Fig. 9: Supplementary Figure: Growth of classical computation cost towards the weak coupling limit. For a fixed system size and the fixed Hamiltonian encoded in MPO or the quantum circuit with a fixed gate depth, the computation time increases as the coupling constant x increases. Clock time for computing each Trotter step of the TN calculation on a Mac Pro tower (3.2GHz 16-core 4.4GHz Intel Xeon W processor, 96GB) is presented in the left panel. Compute time for Pauli propagation using HP Z2 Tower G9 Workstation id presented in the middle panel. PP on NVIDIA RTX 5000 Ada GPU(AD102GL) in presented in the right panel.

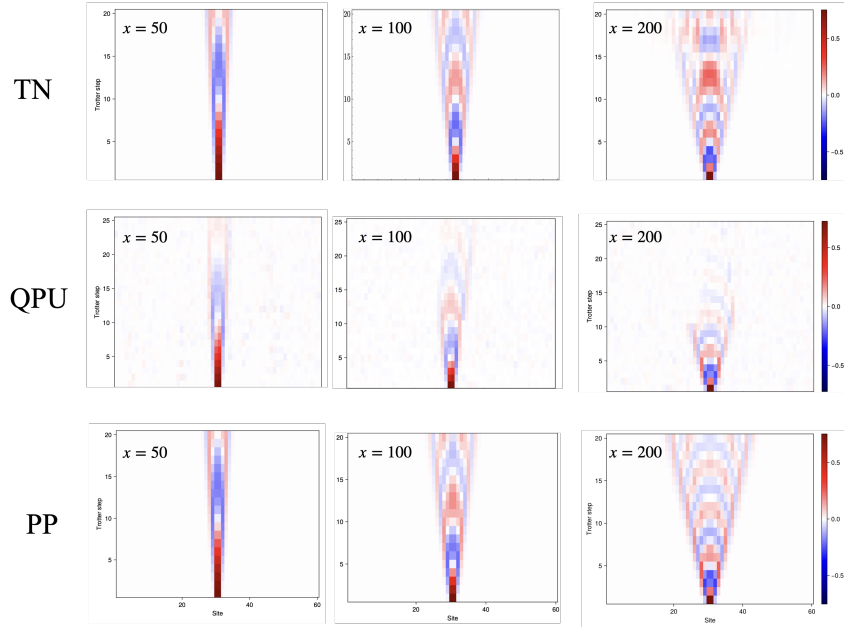


Fig. 10: Supplementary Figure: Probing high fidelity dynamics for different parameter values. The quantum simulation protocol is further tested for a couple of different values of coupling $x = 50$ and $x = 200$, without changing the value of m/g as presented in Fig. 6. The robustness of QPU performance is evident in the consistently increasing width of the lightcone as x increases, which is consistent with the classical simulation as well. QPU results for 25 Trotter steps are presented in the middle panel. It is clear that noise dominates at later times as the 2-qubit gate depth increases to 324 at the 25th step. The signal still appears coherent for $x = 50, 100$, while the contrast decays with time. The top panel shows the result obtained via tensor network calculations for a time equivalent to 20 Trotter steps. For $x = 100$, The TN calculation breaks down beyond 20 Trotter steps for $x = 100$ (not shown in the figure), while the same for $x = 200$ is manifest in the top right plot right after 10th time slice. The PP-CPU result for all three values of x provides the simulated noiseless outcome from QPU with proper estimation of the maximum number of terms. The mismatch between Pauli propagation result and tensor network result allows one to identify when the latter method breaks down (evident for $x = 200$, $N_\tau > 10$).

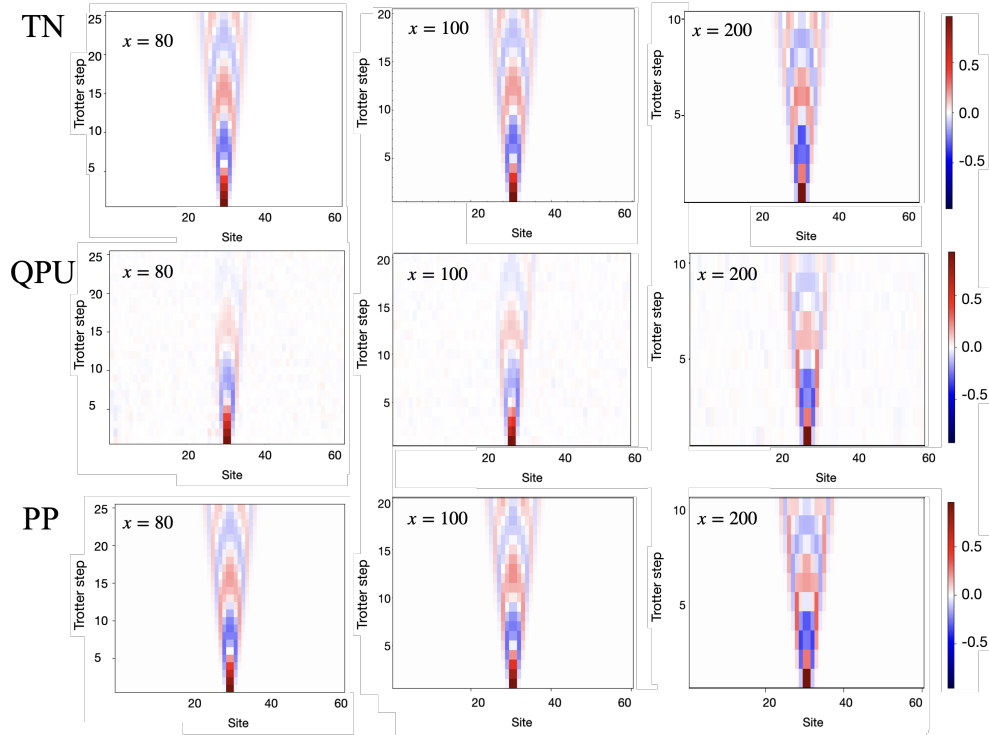


Fig. 11: Supplementary Figure: Robust quantum simulation upto the same physical time. Once studied for the same physical time, for different values of the coupling x , the QPU output remains robust. The above three panels compare dynamics for the same scaled time executed by Trotter steps 25, 20 & 10 for $x = 80$, $x = 100$ & $x = 200$ respectively as obtained by TN, QPU and PP

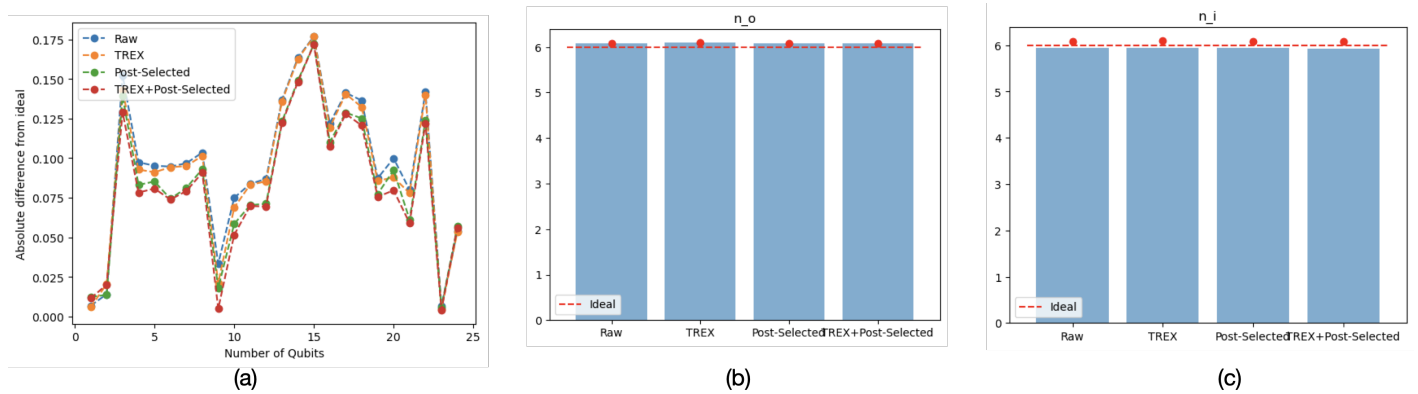


Fig. 12: Supplementary Figure: POC for error mitigation strategy employed. The output from the QPU is presented here with only measurement-error mitigation (TREX). This is decided based on comparing the outcome of simulated noise with the ideal result for a system of 24 qubits. (a) Absolute difference from the ideal result for raw, measurement error mitigation (TREX), post-selection and using both are compared. It appears that TREX alone is able to provide good results. (b), (c) Globally conserved charges stay robust with all the methods.

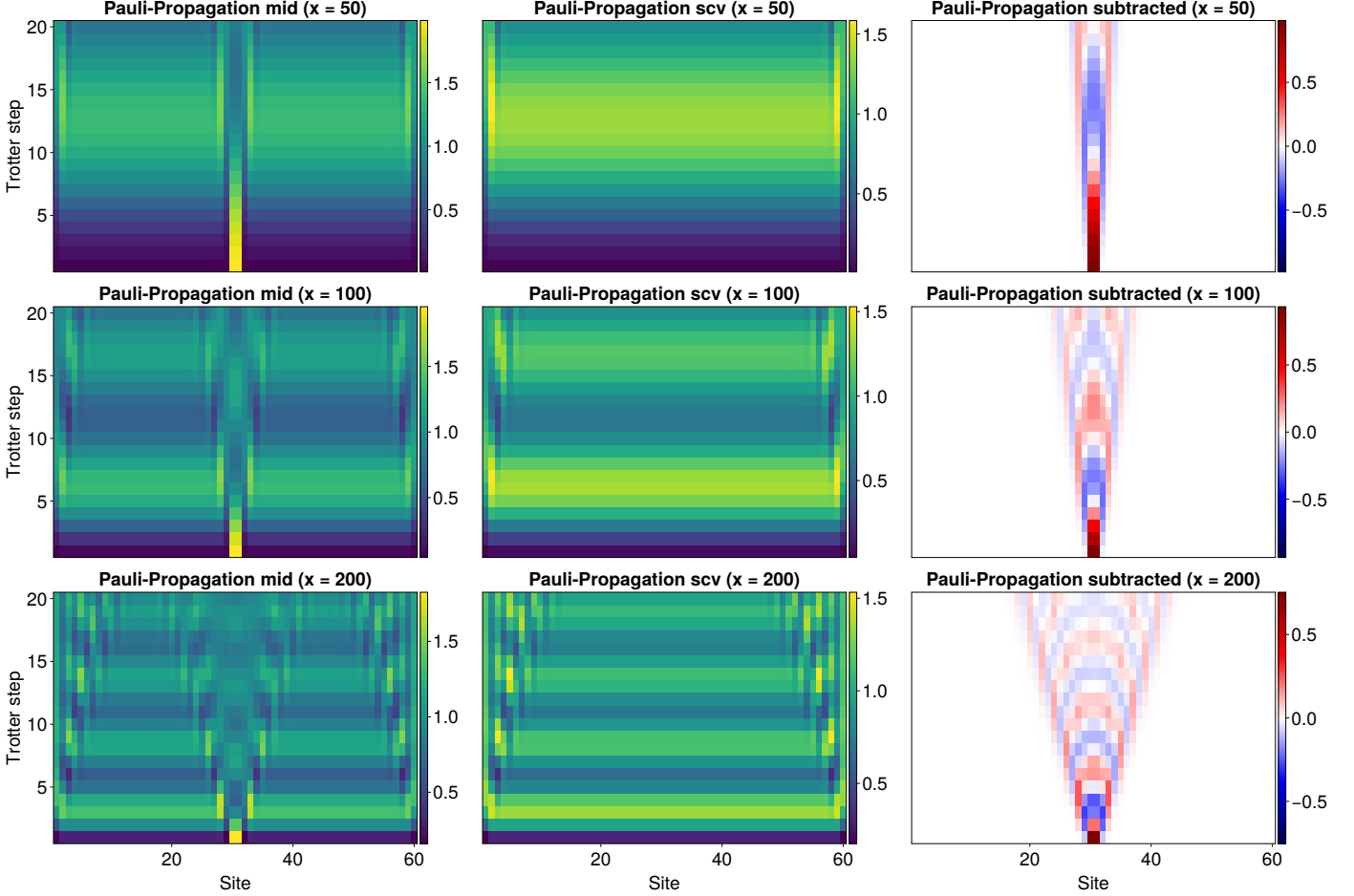


Fig. 13: Supplementary Figure: Demonstrating differential measurement protocol demonstrated for PP. One major reason to obtain reasonably good result only with measurement error mitigation is due to the differential measurement protocol being employed in this work. This protocol cancels some of the systematic error or biases present in the hardware result. In addition, it completely diminishes any boundary effect present in the calculation. As the hadron spreads, performing calculation with a large lattice becomes more and more crucial to avoid any boundary effect. The leftmost column represents propagation of hadron, placed at the center of the finite size lattice for theories with coupling constant $x = 50, 100, 200$. The middle column represents dynamical evolution of the SCV for all three cases. The rightmost column represents the difference between the first two column, which is presented as the result in this current work. It is evident that boundary effects dominate for larger value of x , and hence working with a large lattice is crucial to approach $x \rightarrow \infty$ limit. While this demonstration is with the simulation of noiseless circuit, for the experimental measurement on noisy hardware, some systematic error, mostly if any bias is present gets cancelled and in effect high fidelity results are obtained without active error mitigation.